Deformation-induced domains in silicone rubber

M. O. Bozkurt[a], Z. Hooshmand-Ahoor[a], S. Das[a,b] and V. S. Deshpande[a]

[a]Department of Engineering, University of Cambridge, Trumpington Street, Cambridge CB2 1PZ, UK
[b]Solid Mechanics Division, Department of Applied Mechanics & Biomedical Engineering, IIT Madras, Chennai 600036, India

Abstract

In-situ X-ray computed tomography observations show the development of spatially heterogeneous deformation in cylindrical silicone rubber specimens subjected to a spatially uniform axial strain. Using a doping agent, we demonstrate that this heterogeneity is associated with the motion of a mobile phase within the silicone rubber. The mobile phase is hypothesised to behave like a liquid crystal, with heterogeneity driven by the formation of nematic domains within it. A constitutive model for the deformation of a rubber with such a mobile phase is presented and analysed for axisymmetric uniaxial loading. An important outcome of this analysis is a phase map showing three regimes of behaviour under uniaxial deformation. Spatial heterogeneity develops due to a switch in the orientation of the mobile phase molecules, resulting in the formation of mechanically induced domains within the rubber. Consistent with observations, the model predicts that imposed tensile strains can result in volume loss in the core of the cylindrical specimen and dilation in the outer shell, whereas imposed compressive axial strains reverse this trend.

Keywords: phase formation, hyperelasticity, rubber, X-ray observations

1. Introduction

Silicone rubber has been extensively investigated in the literature, starting from the pioneering works of Mooney (1940) and Rivlin (1948). The behaviour of silicone rubber falls within the broad class of mechanical behaviour of solids known as rubber elasticity. Such solids have the capacity to sustain very large deformations followed by complete recovery and this behaviour is mainly exhibited by polymeric substances comprising predominantly long molecular chains. Detailed molecular theories (Flory and Rehner, 1943; Flory, 1944; James and Guth, 1943, 1944; Treloar, 1943a, 1943b; Arruda and Boyce, 1993) for such materials have been established and supported by macroscopic measurements (Mooney, 1940; Rivlin and Saunders, 1951; Treloar, 1944). The defining feature of models of rubber elasticity is that the Helmholtz free-energy is a function of only temperature and deformation and no other state variable. Recent observations by Wang et al. (2024), however, suggest that under certain conditions silicone rubber might not obey this usual notion of rubber elasticity.

Many synthetic rubbers are synthesised by a polymerisation and/or crosslinking reaction which transforms the highly viscous polymer into an insoluble rubber-like solid. Typically, the crosslinking or curing reaction is initiated by addition of a curing agent or a catalyst. Peroxide, condensation, and addition curing are the three mechanisms by which silicone can be crosslinked (Harkous et al., 2016; Mazurek et al., 2019). The commercial silicone rubber employed by Wang et al. (2024) was a two-part condensation curing silicone. The silane crosslinker and catalyst were packaged together as one reactive component, with the mixture of polymer and filler as the second unreactive component. Once mixed they produced a crosslinking reaction. Wang et al. (2024) demonstrated that under certain conditions there exists a mobile phase within the polymerised rubber presumably because the crosslinking was not complete (Jia et al., 2004; Long et al., 2018). This physics is absent in the classical models for rubbers. Specifically, the mobile species add extra state variables to the Helmholtz free-energy function.

Wang et al. (2024) conducted detailed three-dimensional (3D) measurements of the volumetric deformation fields using X-ray based digital volume correlation (DVC) (Bay et al., 1999; Bay, 2008; Buljac et al., 2018; Jose et al., 2025). These measurements revealed features in deformation of rubbers not previously observed using more standard indentation measurements (Scott et al., 2004; Deuschle et al., 2008). The DVC measurements revealed local volumetric strain distributions with apparent physical inconsistencies if interpreted using usual hyperelastic theories. Including an extra state variable for the concentration of the mobile species and accounting for the motion of these species under imposed deformation reconciled the observations within a classical thermodynamics framework. However, Wang et al. (2024) ignored the possibility of domain formation that is also expected under these conditions.

1.1 Summary of the anomalous behaviour of silicone rubber

Using a combination of X-ray based DVC for 3D volumetric displacement field measurements Wang et al. (2024) demonstrated that certain forms of silicone rubber exhibit significant local volume changes (±10%) over millimetre length scales, but the overall specimen remains incompressible. For example, consider their 4-point bend experiment (Fig. 1a) of a beam of height $2h$ with the associated distribution of $\det(F_{ij})$ at an imposed normalised curvature $\kappa h = 0.24$ shown in Fig. 1b. Here F_{ij} is the material point deformation gradient calculated from the measured 3D displacement fields. While significant local volumetric strains are observed, averaging over the entire specimen volume gives a value $\langle \det(F_{ij}) \rangle = 1.01$. This suggests that to within measurement error the overall specimen is incompressible. Such a surprising response was also observed in other loading situations suggesting that this curious response of local volumetric changes but global incompressibility is connected to the physics of the deformation of the silicone rubber.

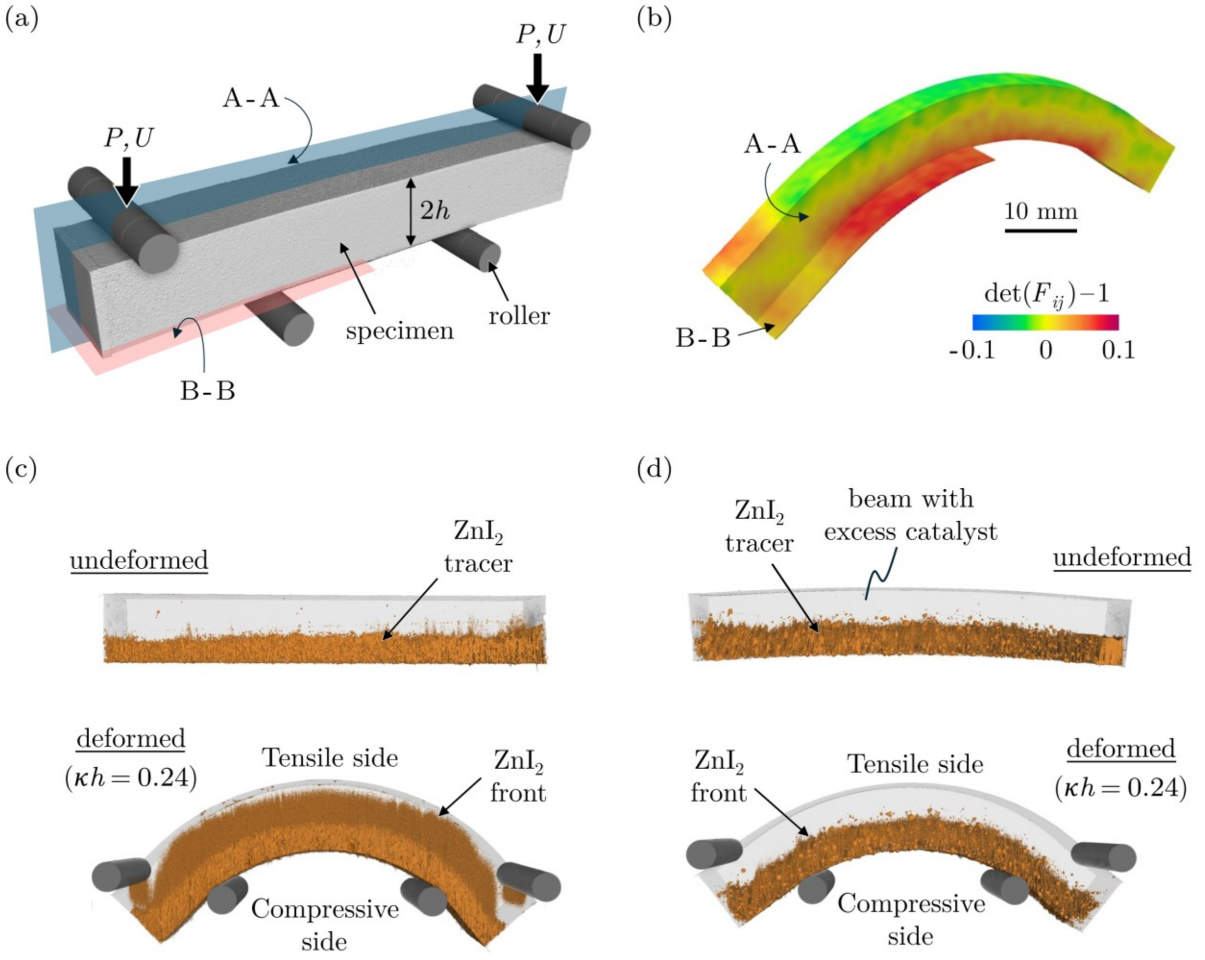

Figure 1: Summary of the key observations of Wang et al. (2024) for the 4-point bend loading of a silicone rubber beam of height $2h$. (a) Sketch of the 4-point bending setup. (b) Measurements of the spatial distribution of the volumetric strain parameterised by $\det(F_{ij})$ upon loading the beam to a normalised curvature $\kappa h = 0.24$. Internal deformation is shown by sectioning the beam on plane A-A and B-B indicated in (a). (c) An undeformed silicone rubber beam with $\mathrm{ZnI_2}$ added as a tracer for the mobile phase molecules. The tracer is only added on the one side of the neutral axis. The distribution of the tracer after loading the beam to $\kappa h = 0.24$ with the initial tracers on the compressive side. (d) A similar tracer experiment with an excess of catalyst added to the silicone rubber to nearly eliminate the mobile phase. The tracer is now seen to not diffuse into the tensile side.

The observations in Fig. 1b are even more curious when we observe that volumetric compression occurs on the tensile side while dilation occurs on the compressive side. Viewed in terms of hyperelasticity, this suggests an apparent negative bulk modulus which is inconsistent with the fact that silicone rubber is a stable solid. Wang et al. (2024) rationalised this inconsistency by hypothesising that there exists a mobile phase within the silicone rubber. By adding a tracer ($\mathrm{ZnI_2}$) to the silicone rubber they observed the motion of the mobile phase within the silicone rubber beam (Fig. 1c). The mobile phase was hypothesised to be associated with an incomplete polymerisation/cross-linking reaction. To test this hypothesis, Wang et al. (2024) manufactured silicone rubber beams with excess catalyst (curing agent) added to the silicone rubber base. This was expected to eliminate the mobile phase by completing the polymerisation/cross-linking reaction. The observation that the $\mathrm{ZnI_2}$ tracers were immobile in these silicone rubber beams with excess catalyst (Fig. 1d) confirmed the notion of an incomplete polymerisation/cross-linking reaction being the source of the mobile phase. Combining the notion of a mobile phase with the assumption that the mobile molecules induce an anisotropic swelling strain in the rubber, they constructed a thermodynamic framework to rationalise the observations including the apparent negative bulk modulus.

The anisotropy of the swelling strains is a direct consequence of the directionality of the mobile phase molecules. These mobile molecules not only move within the rubber but can also re-orient. This opens the possibility of mechanically-induced domain formation within the mobile phase. This has analogies with nematic domain formation in liquid crystals (Williams, 1963; Stephen and Straley, 1974; Küpfer and Finkelmann, 1991; Bladon et al., 1994; Zubarev et al., 1999; Zhang et al., 2020; Zhao et al., 2023). Wang et al. (2024) did not discuss this possibility in their analysis or observations. The aim of this study is to investigate the possibility of nematic domain formation and develop a framework to predict deformation-induced domain formation in rubbers.

2. Evidence of domain formation in silicone rubber

The model of Wang et al. (2024) assumes anisotropic swelling induced by the mobile phase molecules. The directionality associated with this anisotropic swelling thus depends on the orientation of the mobile phase molecules and accordingly, we can define a phase of the silicone rubber that depends on the orientation of the mobile molecules. Wang et al. (2024) only analysed pure bending loading where the mobile molecules are similarly orientated throughout the domain, i.e. there is no texture or domain formation within a beam under pure bending. An open question is therefore whether mechanical loading can induce different phases/domains of the mobile molecules in a single specimen.

Consider a cylindrical silicone rubber specimen of height H and diameter D with top and bottom surfaces glued to platens (Fig. 2a). Such a cylinder of aspect ratio $H/D = 1$ ($D = 28\,\mathrm{mm}$) is then subjected to uniaxial compression. Following the procedure of Wang et al. (2024) we conducted in situ computed X-ray tomography measurements along with DVC at three levels of the applied compressive displacement U with the experiment spanning ~5 hrs. Select components of the deformation gradient F_{ij} are shown in Fig. 2b at three levels of the applied U/H. Now consider the symmetric central plane of the specimen indicated by A-A in Fig. 2b. The axial component F_{33} of the deformation gradient is spatially uniform over this plane (Fig. 2c), but the in-plane component F_{11} is not. The shear component $F_{13} \approx 0$ consistent with the symmetry of the imposed loading. Consequently, $\det(F_{ij})$ is not uniform over the central cross-section (Fig. 2c). This is somewhat surprising as we now proceed to explain. Consider a cylinder subjected to uniaxial compressive loading with spatially uniform axial strain. A homogeneous material will respond uniformly in this statically determinate situation with all components of the strain (or deformation gradient) being spatially uniform. Thus, given the uniform F_{33} on the central plane we would have anticipated F_{11} (and $\det(F_{ij})$) to be spatially uniform on the central plane. The fact that it is not in the nominally homogeneous silicone rubber is the surprise. One explanation is that deformation-induced texture generates spatially heterogenous mechanical properties.

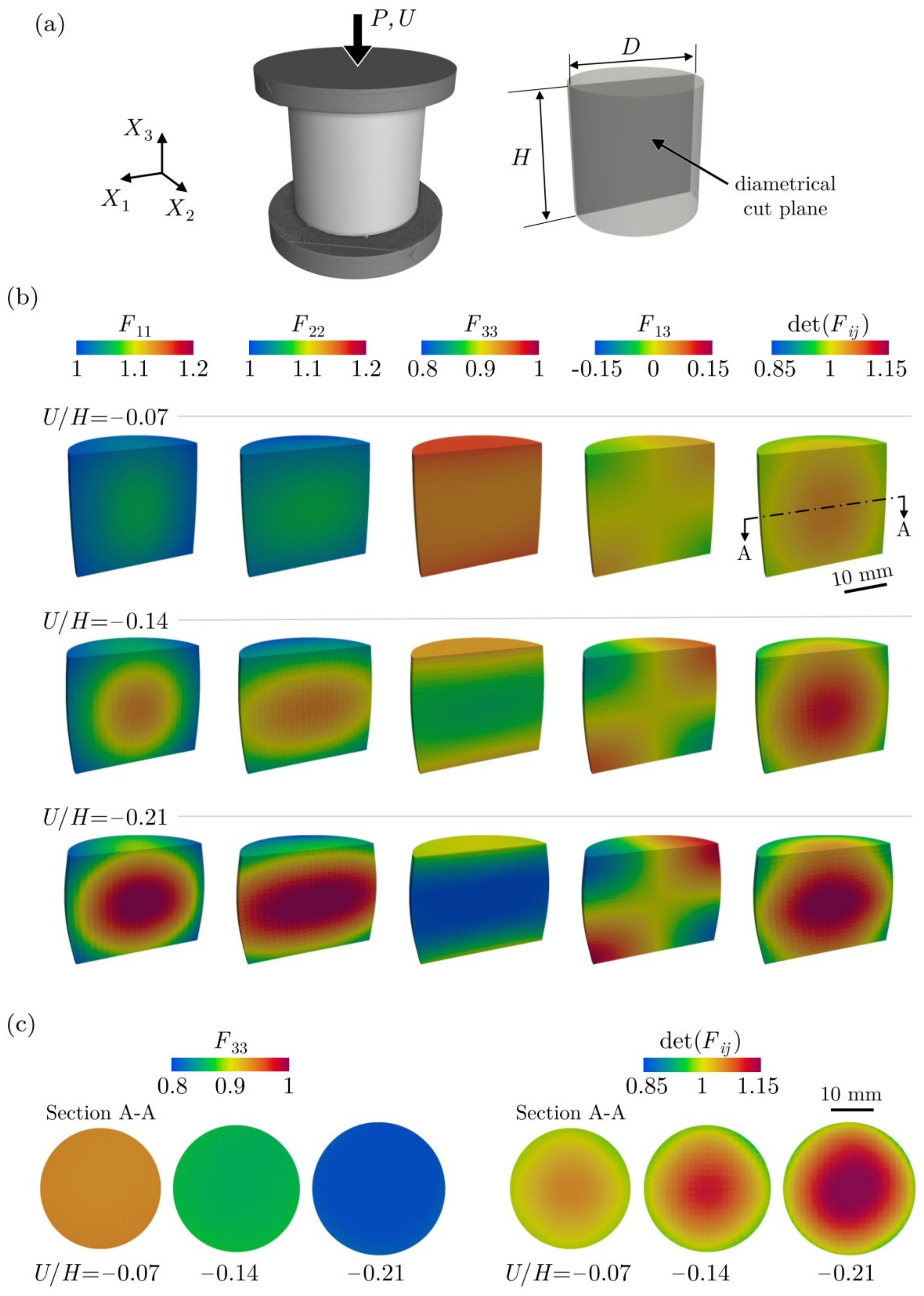

Figure 2: (a) Sketch of the compressive loading of a cylindrical specimen with top and bottom surfaces glued to platens. The global coordinate system X_i is also shown. (b) Spatial distribution of select components of F_{ij} and $\det(F_{ij})$ of the $H/D = 1$ specimen subject to compressive loading. The distributions are shown on the diametrical plane indicated in (a) at three levels of the applied nominal compressive strain U/H. (c) Distributions of F_{33} and $\det(F_{ij})$ on the central symmetry plane A-A indicated in (b) for the same three levels of U/H.

In the context of the model of Wang et al. (2024), texture is induced by the reorientation of the mobile phase molecules. While we cannot directly observe this reorientation, we look for other signatures to show that the observed spatially inhomogeneous deformation is associated with the mobile phase. Recall that under uniaxial compression, there will be no spatial gradients and hence no driving force for the motion of the mobile phase. Motion of the mobile phase will suggest that the spatial inhomogeneity is associated with the mobile phase. Following Wang et al. (2024) we repeated the experiment of Fig. 2 by now adding tracers to detect the motion of the mobile phase.

2.1 Compression with added tracers

We briefly describe the experimental protocol that follows closely that of Wang et al. (2024). The two-part Polycraft GP3481-F RTV mould-making silicone rubber comprises the Polycraft base which when mixed with the Polycraft red fast set catalyst results in a room temperature condensation curing reaction. The base and catalyst were mixed in ratio 20:1 (by weight) and poured into a Perspex mould to produce a cylindrical specimen of diameter $D = 28$ mm and height $H = 28$ mm. The pouring was performed in 3 stages. After each casting stage, the partially cast specimen was cured for ~10 h at 4 °C to slow the curing process and prevent mixing between the layers, while ensuring a uniform bond between them.

(i) The mixture comprising just the base and catalyst was poured into the mould to a height of 13 mm, i.e. 1mm below the central plane of the specimen.
(ii) Next, a mixture comprising the base with 3% by wt. $\mathrm{ZnI_2}$ particles mixed with the catalyst was poured into the mould to increase the height of the specimen by 2 mm.
(iii) Finally, again a mixture comprising just the base and catalyst was poured into the mould to create a specimen of height $H = 28$ mm.

The final cast specimen was then cured for 48 hrs at 4°C to slow the curing process. This allowed any trapped air bubbles to escape. The sample was de-moulded after a further-one day of curing at room temperature. The specimen was then glued to Perspex platens ready for testing.

The specimen was placed inside a custom-built in situ loading setup (Wang et al., 2024) and X-ray tomographs were obtained using the Nikon XTH 225 ST system; see Appendix A for details. First consider the undeformed specimen. A histogram of the grey values of the scan is included in Fig. 3a with the materials corresponding to the different peaks labelled. The tomograph of the undeformed specimen with the $\mathrm{ZnI_2}$ coloured is included in Fig. 3b: consistent with the specimen manufacture described above, the $\mathrm{ZnI_2}$ exists in a disc of height ~2 mm centred about the central symmetry plane of the specimen. A slight non-uniformity is present initially in this thin $\mathrm{ZnI_2}$ layer with capillary effects at the mould walls resulting in the $\mathrm{ZnI_2}$ layer being thinner towards the centre of the cylinder. This specimen was then compressed to a compressive strain $U/H = -0.2$ and the tomograph was repeated with the specimen under load. A comparison of the tomographs of the undeformed and deformed specimens (Fig. 3b) shows a clear difference of the $\mathrm{ZnI_2}$ structure: $\mathrm{ZnI_2}$ seems to be depleted towards the centre of the specimen. To illustrate this more clearly, we include in Fig. 3c two views of the central section of the undeformed and deformed specimens. These images demonstrate that imposing uniaxial compression on the central disc results in motion/rearrangement of the mobile phase. We note in passing that removal of the applied deformation resulted in the $\mathrm{ZnI_2}$ returning to the original undeformed spatial distribution confirming that the rearrangement is deformation-induced. This rearrangement is expected to cause deformation-induced heterogeneity which might explain the spatially non-uniform straining of this disc seen in Fig. 2b. The key aim of this study is to understand how imposition of uniaxial compression results in this heterogeneity.

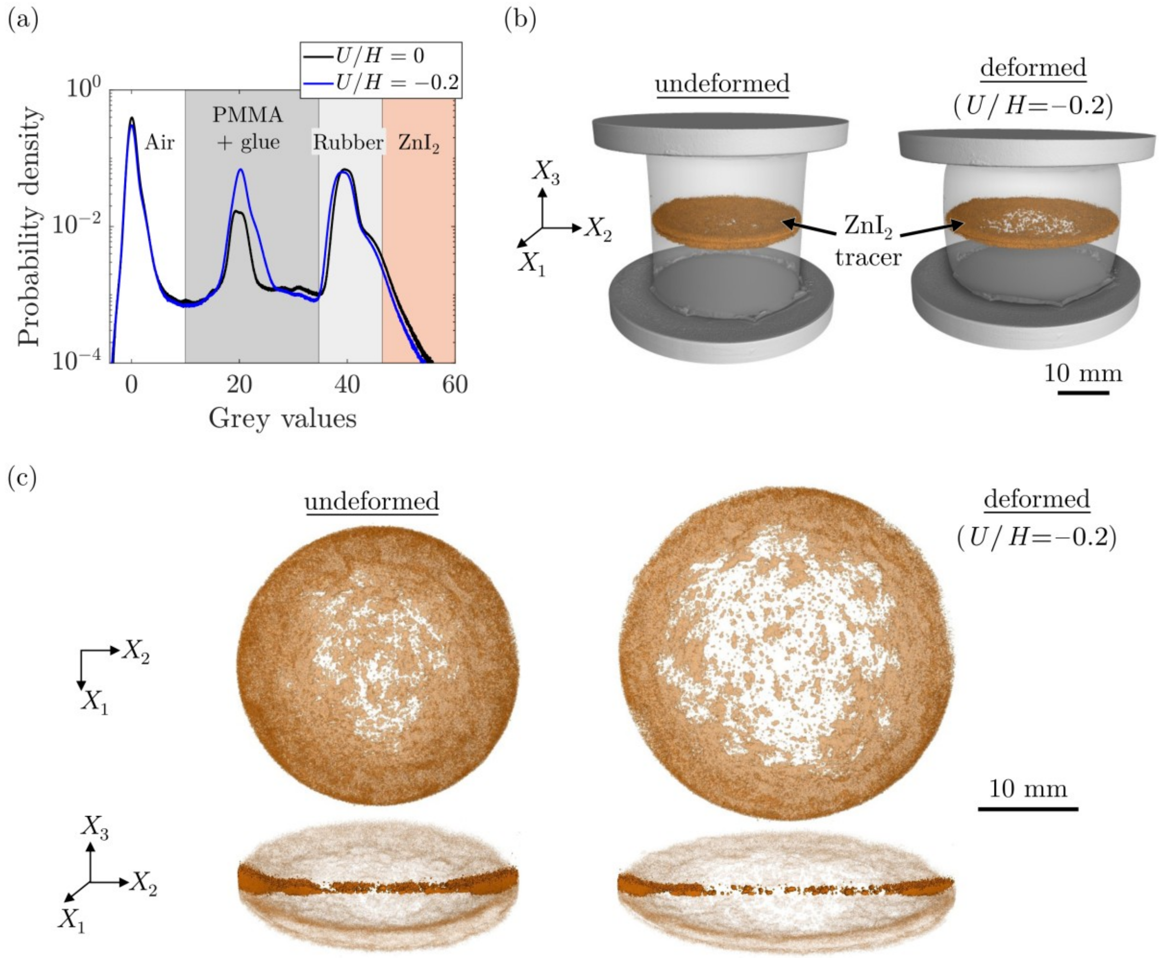

Figure 3: Compressive loading of the $H/D = 1$ cylindrical specimen with tracers added on the central plane. (a) The grey value histograms of the undeformed specimen and specimen deformed to a compressive displacement $U = -0.2H$. The different materials as distinguished by their grey values are indicated. (b) 3D views of the distributions of the ZnI_2 tracers (coloured in brown) within the undeformed specimen and specimen deformed to $U = -0.2H$. (c) Corresponding top and side section views of the central plane of deformed and undeformed specimens.

3. Summary of constitutive model for silicone rubber with a mobile phase

Before proceeding to analyse the deformation-induced heterogeneity described above, we briefly summarize the model of Wang et al. (2024) in the small strain context. The model includes a mobile phase with anisotropic swelling caused by the motion of this mobile phase and we include minor modifications in the calculation of the orientation of the mobile phase molecules and in the free-energy they proposed. These modifications were needed to ensure that the model remains well-posed while predicting domain formation.

In addition to temperature $\mathcal{T}$, the Helmholtz free-energy is written in terms of three state variables: (i) the total strain ε_{ij}, (ii) the molar concentration c (per unit volume of the rubber) of the mobile phase and (iii) the orientation of the mobile molecules denoted by ℓ. Let c_R denote the molar concentration of the sites for the mobile phase molecules and we define an occupancy $\xi \equiv c/c_R$ (with $\xi = \xi_0$ in the reference state) of these sites. This mobile phase induces an anisotropic "swelling" strain when $\xi \neq \xi_0$. We first discuss the non-standard choices of the swelling strains proposed by Wang et al. (2024) to rationalise their observations and then proceed to describe the constitutive model. Denote the swelling strain ε^s_{ij} as a function of the concentration c and the orientation ℓ of the mobile phase molecules. Incompressibility of the overall specimen requires that the volumetric swelling strain ε^s_{ii} is linear in c (Wang et al., 2024) such that

$$\varepsilon^s_{ii} = k(\xi_0 - \xi), \tag{3.1}$$

where $k \geq 0$ is a coefficient relating occupancy to strain. We observe that increasing ξ above the reference value of ξ_0 results in volume loss due to swelling. This non-standard choice was motivated by the observation that while the motion of the mobile phase molecules was from the compressive to tensile side of the beam (Fig. 1c), volume reduction was observed on the tensile side. The non-standard choice (3.1) is physically rationalised as follows. The mobile phase presumably exists within nano capillaries in the cross-linked rubber. Increasing the "liquid" mobile phase results in collapse of these elastic capillaries via surface tension with a consequent volume loss with increasing concentration as parameterised by (3.1).

The mobile phase molecules are assumed to be ellipsoidal and inducing principal strains aligned with the principal axes of the molecules. Thus, two of the swelling strains are equal and Wang et al. (2024) proposed that the three principal swelling strains $e^{[p]}$ are given by

$$e^{[1]} = e^{[2]} = k(\xi_0 - \xi), \quad e^{[3]} = -k(\xi_0 - \xi), \tag{3.2}$$

such that $(e^{[1]} + e^{[2]} + e^{[3]}) = k(\xi_0 - \xi)$ consistent with (3.1). Then, given the directions $q_k^{[p]}$ ($p = 1,2,3$) of $e^{[p]}$ it follows that $\varepsilon^s_{kj} q_j^{[p]} = e^{[p\,]} q_k^{[p]}$. The total strain ε_{ij} is additively decomposed into an elastic component ε^e_{ij} and the swelling component such that $\varepsilon_{ij} = \varepsilon^e_{ij} + \varepsilon^s_{ij}$. The Helmholtz free-energy f per unit volume of the silicone rubber is then written in terms of the first and second Lamé parameters λ and G, respectively and the universal gas constant $\mathcal{R}$ as

$$f\left(\varepsilon_{ij}, c, \ell, \mathcal{T}\right) = \left[\lambda/2(\varepsilon^e_{kk})^2 + G\varepsilon^e_{ij}\varepsilon^e_{ij}\right] + \mathcal{R}\mathcal{T}c_R[\xi \ln \xi + (1 - \xi)\ln(1 - \xi)] + f_{\text{reg}}, \tag{3.3}$$

with a regularisation term f_{reg} added to ensure the response follows the isotropy of the loading (see Appendix B for further details on this regularisation). We emphasise that f_{reg} is designed such that $f_{\text{reg}} = 0$ when f is minimised. In (3.3) the first term is the elastic energy of the backbone cross-linked polymer network while the second term is the configuration entropy of the mobile phase.

The observation (Fig. 2b) that the central plane of the compressed silicone rubber cylinder remains a plane of symmetry motivates a constitutive assumption for the directions $q_k^{[p]}$. The observed symmetry in Fig. 2b implies that the radial, tangential and axial directions, viz. (r, θ, z) are principal directions of ε_{ij}. This strongly suggests that the principal directions $q_k^{[p]}$ of the swelling strains are aligned with the principal directions $n_k^{[m]}$ ($m = 1,2,3$) of the total strains ε_{ij}. Therefore, a descriptor ℓ for the orientation of the mobile molecules assumes discrete values which we take to be $\ell = 0,1,2$ to specify the alignment of the molecular directions $p = 1,2,3$, as specified in (3.2), with the three principal directions $m = 1,2,3$ of the total strains. Then ℓ, $q_k^{[p]}$ and $n_k^{[m]}$ are related in modular arithmetic[1] notation via

---

[1] Modular arithmetic is the system of arithmetic for integers where the numbers "wrap around" when *exceeding* a certain value, called modulus. For example, in a 12-hour clock if it is 7:00 now in 8 hours it will be 3:00 since the clock "wraps around" every 12 hours. Thus, in (3.4) if $p = 3$ & $\ell = 2$; $p + \ell \pmod 3 = 2$.

$$q_k^{[p+\ell\ (\mathrm{mod}\ 3)]} = n_k^{[p]}. \tag{3.4}$$

We now proceed to complete the description of the response of the silicone rubber with this mobile phase. Recall that our measurements spanned a duration of ~ 5 hrs. The observations of Wang et al. (2024) show that the mobility of the mobile molecules is very high, such that they move ~2.7 mm in 4 s (corresponding to an inferred linear diffusion co-efficient of 1.8 $\mathrm{mm}^2\ \mathrm{s}^{-1}$). Thus, in our slow experiments the silicone rubber specimens would be in a state of equilibrium throughout the loading, and we present such an equilibrium analysis that neglects the kinetics of the motion of the mobile phase.

First, we define two conjugates to the variables defining f, viz. the material stress

$$\sigma_{ij} \equiv \left.\frac{\partial f}{\partial \varepsilon_{ij}}\right|_{c,\ell,\mathcal{T}}, \tag{3.5}$$

and the chemical potential of the mobile species

$$\mu \equiv \left.\frac{\partial f}{\partial c}\right|_{\varepsilon_{ij},\ell,\mathcal{T}}. \tag{3.6}$$

Then to define the equilibrium state of the rubber, we define the potential energy Π of the rubber specimen occupying a domain Ω subjected to surface tractions $T_i = T_i^0$ on a portion S_T and displacements $u_i = u_i^0$ on a portion S_U of the boundary S of the domain Ω. The potential energy of this system is then

$$\Pi(u_i, c, \ell) = \int_\Omega f d\Omega - \int_{S_T} T_i^0 u_i dS, \tag{3.7}$$

and at equilibrium Π is minimised. Taking the variation with respect to u_i gives the usual mechanical equilibrium relation $\sigma_{ij,j} = 0$ with boundary conditions $T_i^0 = \sigma_{ij} m_j$ on S_T where m_j is the outward normal to S_T and $u_i = u_i^0$ on a portion S_U. Further taking the variation of (3.7) with respect to c and recalling that the total amount of the mobile phase in the specimen is a constant (i.e., the mobile phase does not leave or enter the specimen) we observe that at equilibrium the chemical potential is a constant such that $\mu = \mu_0$ with μ_0 set by the conservation condition $\int_\Omega c d\Omega = c_R \xi_0 \Omega$. Finally, we need to find the equilibrium condition with respect to ℓ. However, ℓ is a discrete variable taking integer values $\ell = 0,1,2$, and thus we cannot take arbitrary variations of Π with respect to ℓ. Therefore, the equilibrium condition with respect to the orientation of the mobile phase molecules is best expressed as the minimisation of (3.7) with respect to ℓ. Let $\Psi(\ell(x_i))$ denote the value of Π for a given distribution of $\ell(x_i)$ such that $\sigma_{ij,j} = 0$ with $T_i^0 = \sigma_{ij} m_j$ on S_T and $u_i = u_i^0$ on S_U and μ is constant throughout Ω with $\int_\Omega c d\Omega = c_R \xi_0 \Omega$. Then at overall equilibrium the potential energy is given by

$$\Psi_{\min} = \min_{\ell} \ \Psi, \tag{3.8}$$

with $\ell_{\min}$ denoting the distribution corresponding to $\Psi_{\min}$. We note that this specification of $\ell(x_i)$ obtained by the minimisation of (3.7) with respect to the discrete variable ℓ differs from that discussed by Wang et al. (2024) who suggested that ℓ can be obtained by a minimisation of the elastic energy.

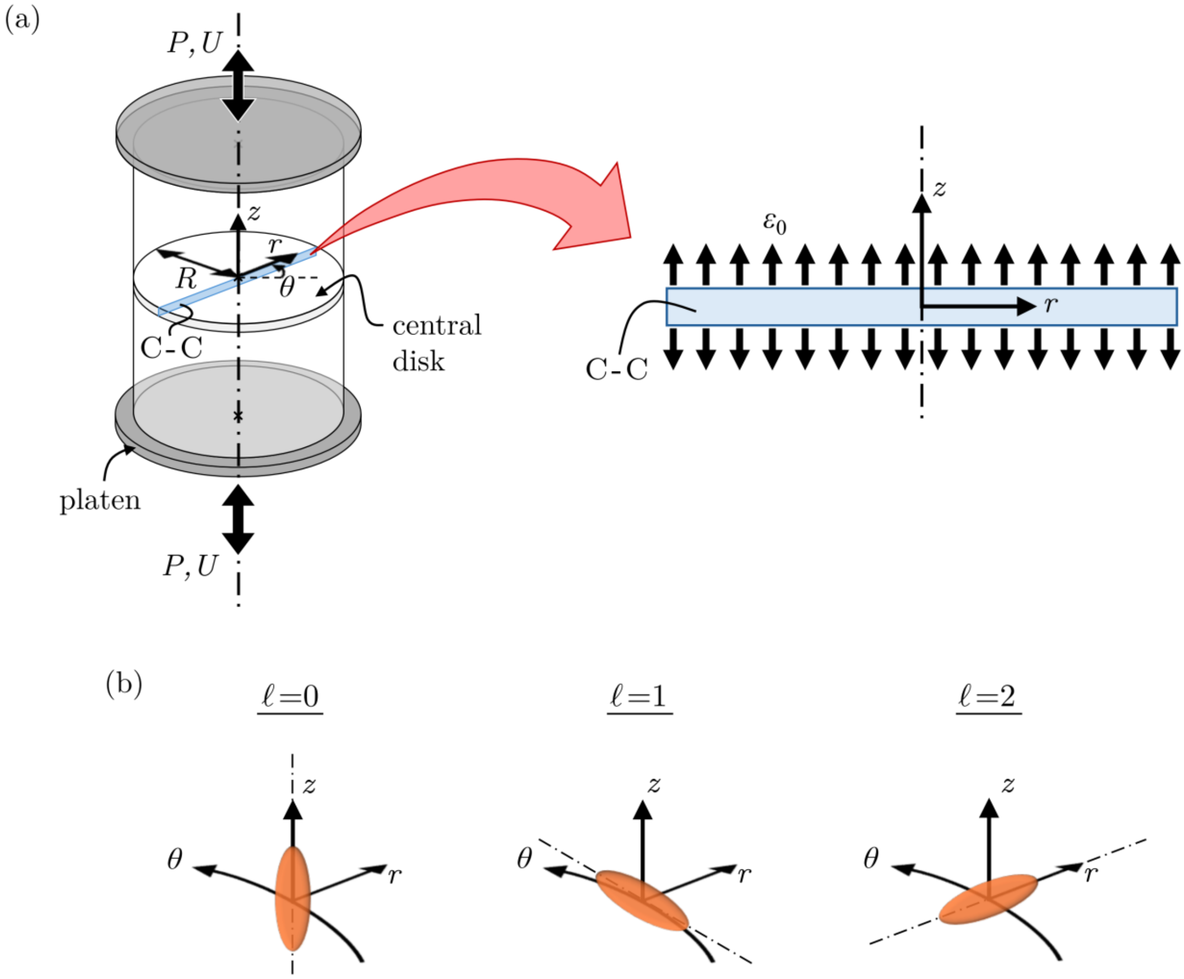

Figure 4: (a) Sketch of the tensile/compressive loading of the cylindrical specimen with top and bottom surfaces glued to platens. We analyse a thin central disc subjected to a spatially uniform axial strain ε_{zz} and constrained to deform axisymetrically. The axisymmetric co-ordinate system (r, θ, z) is indicated. (b) Sketch illustrating the three orientations $\ell \in \{0,1,2\}$ of the ellipsoidal mobile phase molecules with respect to (r, θ, z) directions.

4. Analysis of uniaxial deformation

The central plane in the compression test detailed in Section 2 has zero shear strain and a uniform imposed axial strain. Thus, this central plane is under uniaxial compression. However, the results of Section 2 strongly suggest that imposition of uniaxial compression results in the development of deformation-induced heterogeneity. This motivates us to examine the central disc of the cylinder under uniaxial deformation.

We analyse the behaviour of a thin central disc (Fig. 4a) of radius R. Consistent with observations (Fig. 2b) this disc is subjected to a spatially uniform axial deformation $\varepsilon_{zz}(r) = \varepsilon_0$. The mobile phase can flow between this disc and the rest of the silicone rubber specimen and thus without analysing the full cylinder, the average occupancy

$$\langle \xi \rangle \equiv \frac{2}{R^2} \int_0^R \xi \, r dr \tag{4.1}$$

within the disc is unknown. In our analysis here, we treat $\langle \xi \rangle$ as a "loading" parameter in addition to the imposed axial strain ε_0. This allows us to investigate the formation of heterogeneity as a function of $(\varepsilon_0, \langle \xi \rangle)$. Consistent with the observations we restrict the analysis to axisymmetric deformation with the co-ordinate system (r, θ, z) illustrated in Fig. 4a. Denoting the radial co-ordinate as r, the axisymmetric analysis exploits the facts:

(i) The shear deformation $\varepsilon_{rz} = 0$ and thus (r, θ, z) are principal directions such that $(\varepsilon_{zz}, \varepsilon_{rr}, \varepsilon_{\theta\theta})$ are principal strains.

(ii) In the thin disc, there is no variation in the axial direction, i.e. all gradient $\partial(\cdot)/\partial z$ vanish.

(iii) The boundary condition is $\sigma_{rr} = 0$ at $r = R$.

Since $(\varepsilon_{zz}, \varepsilon_{rr}, \varepsilon_{\theta\theta})$ are principal strains, it implies that $e^{[p]}$ are aligned along the (z, r, θ) directions, such that the swelling strains can be written as

$$\begin{bmatrix} \varepsilon_{rr}^{s} \\ \varepsilon_{\theta\theta}^{s} \\ \varepsilon_{zz}^{s} \end{bmatrix} = \begin{bmatrix} e^{[(1+\ell) \bmod 3]} \\ e^{[(2+\ell) \bmod 3]} \\ e^{[(3+\ell) \bmod 3]} \end{bmatrix} = k(\xi_0 - \xi) \begin{bmatrix} S^{[(1+\ell) \bmod 3]} \\ S^{[(2+\ell) \bmod 3]} \\ S^{[(3+\ell) \bmod 3]} \end{bmatrix}, \tag{4.2}$$

where $S^{[i]} \equiv \mathrm{sign}\left(e^{[i]}/k(\xi_0 - \xi)\right) = [+1, +1, -1]$ and the principal swelling strains $e^{[i]}$ are given by (3.2). In (4.2) $\ell \in \{0,1,2\}$ corresponds to the 3-directions in (3.2) with the major axis of the mobile phase molecules aligned with the z, θ, and r −directions, respectively as depicted in Fig. 4b. Thus, the only non-zero elastic strains are $(\varepsilon_{zz}^{e}, \varepsilon_{rr}^{e}, \varepsilon_{\theta\theta}^{e})$ and consequently the only non-zero stresses are $(\sigma_{zz}, \sigma_{rr}, \sigma_{\theta\theta})$. This considerably simplifies the analysis and we shall now proceed to describe the solution of the model of Section 3 in this context.

4.1 Mechanical equilibrium

Under axisymmetric deformation with the deformation obeying $\partial(\cdot)/\partial z = 0$, the deformation field within the disc can be completely described in terms of the radial displacement $u(r)$ where $\varepsilon_{rr} = du/dr$ and $\varepsilon_{\theta\theta} = u/r$. Moreover, we do not need to consider the displacement in the z −direction as the imposed strain ε_{zz} is spatially uniform. The mechanical equilibrium equation $\sigma_{ij,j} = 0$ then reduces to the single equation

$$\frac{d\sigma_{rr}}{dr} + \frac{1}{r}(\sigma_{rr} - \sigma_{\theta\theta}) = 0, \tag{4.3}$$

with boundary condition $\sigma_{rr} = 0$ at $r = R$ and the imposed strain $\varepsilon_{zz}(r) = \varepsilon_0$. The stresses are related to the strains via (3.3) and (3.5) via

$$\varepsilon_{rr} = \varepsilon_{rr}^{e} + \varepsilon_{rr}^{s} = \frac{1}{E}[\sigma_{rr} - \nu(\sigma_{\theta\theta} + \sigma_{zz})] + \varepsilon_{rr}^{s}, \tag{4.4}$$

$$\varepsilon_{\theta\theta} = \varepsilon_{\theta\theta}^{e} + \varepsilon_{\theta\theta}^{s} = \frac{1}{E}[\sigma_{\theta\theta} - \nu(\sigma_{rr} + \sigma_{zz})] + \varepsilon_{\theta\theta}^{s}, \tag{4.5}$$

and

$$\varepsilon_{zz} = \varepsilon_{zz}^{e} + \varepsilon_{zz}^{s} = \frac{1}{E}[\sigma_{zz} - \nu(\sigma_{rr} + \sigma_{\theta\theta})] + \varepsilon_{zz}^{s}, \tag{4.6}$$

where we have written the relation in terms of the Young's modulus E and Poisson's ratio ν (which are directly related to the Lamé constants). In (4.4)-(4.6) we have neglected contributions of the regularisation term f_{reg} which is only non-zero when the orientation of the mobile phase molecules does not minimise the free-energy. Thus, in equilibrium solutions f_{reg} does not contribute to the fields.

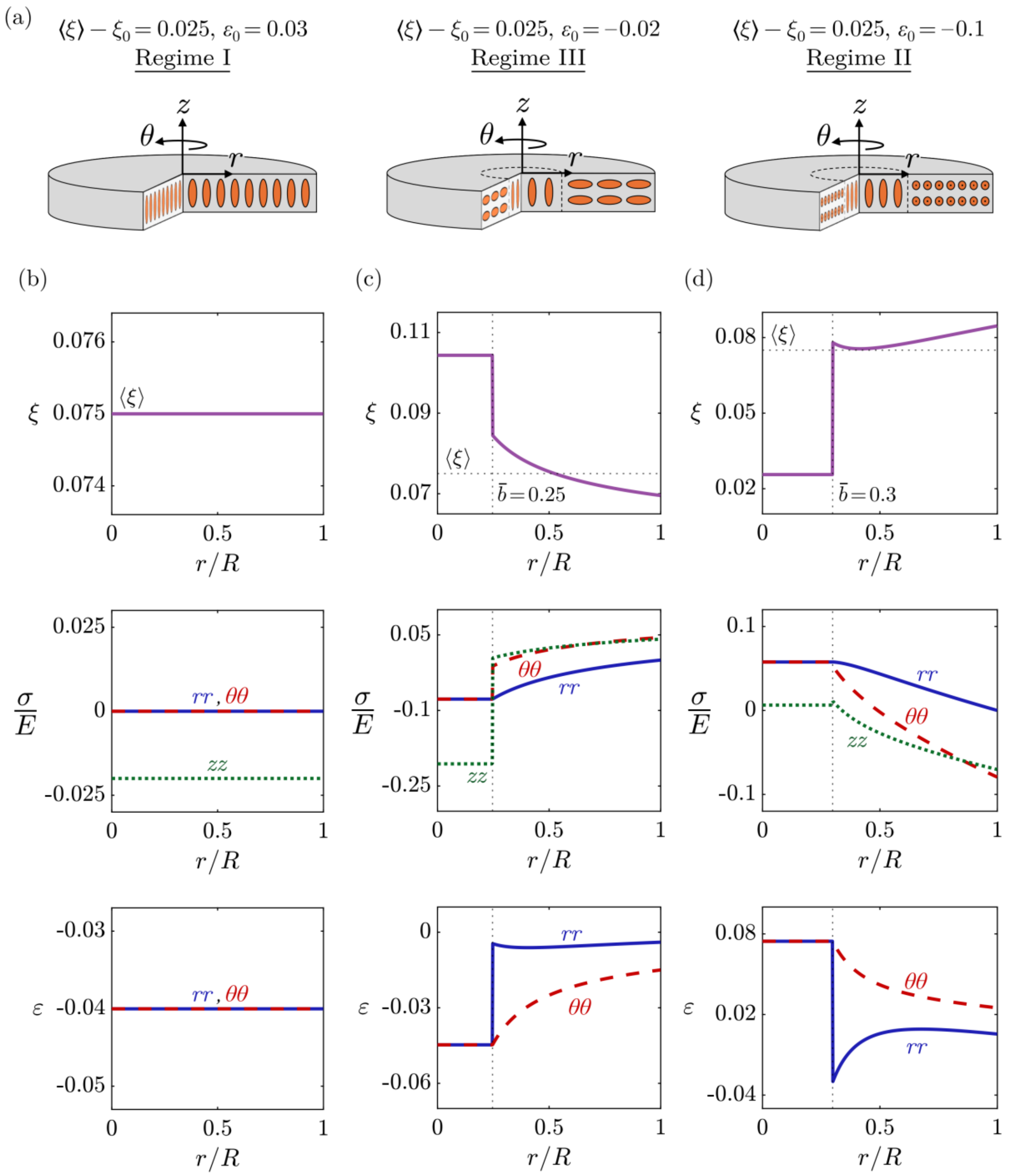

Figure 5: (a) Sketches of the 3 regimes of behaviour for a cylindrical specimen loaded by a combination of an imposed strain $\varepsilon_{zz}(r)=\varepsilon_0$ and average occupancy $\langle\xi\rangle$. (b-d) Predictions of the spatial variation of ξ, the three normalised stresses $(\sigma_{rr}/E, \sigma_{\theta\theta}/E, \sigma_{zz}/E)$, and the total strains $(\varepsilon_{rr}, \varepsilon_{\theta\theta})$ for a disc with occupancy $\langle\xi\rangle-\xi_0=0.025$. The variations are shown as a function of the normalised radial co-ordinate r/R. (b) Regime I with an imposed strain $\varepsilon_0=0.03$. (c) Regime III with an imposed strain $\varepsilon_0=-0.02$. (d) Regime II with an imposed strain $\varepsilon_0=-0.1$.

4.2 Chemical equilibrium

Using (3.3), (4.2), and (4.4)-(4.6), the chemical potential (3.6) in the thin axisymmetric disc is succinctly written as

$$\mu=\frac{k}{c_R}\left(S^{[(1+\ell)\,\mathrm{mod}\,3]}\sigma_{rr}+S^{[(2+\ell)\,\mathrm{mod}\,3]}\sigma_{\theta\theta}+S^{[(3+\ell)\,\mathrm{mod}\,3]}\sigma_{zz}\right)+\mathcal{R}\mathcal{T}\ln\left(\frac{\xi}{1-\xi}\right), \tag{4.7}$$

i.e. μ depends on the orientation of the molecules of the mobile phase. The equilibrium condition is that μ is spatially uniform with its value constrained such that the total amount of the mobile phase is set by the specified value of $\langle\xi\rangle$.

4.3 Types/phases of heterogenous solutions

The mobile phase can exist in orientations $\ell \in \{0,1,2\}$ within the disc as depicted in Fig. 4b. We thus need to determine the distribution $\ell(r)$ at equilibrium following the minimisation condition (3.8). We shall subsequently demonstrate that the solutions are such that finite domains with different values of ℓ form within the disc.

First consider a constraint on the solution in the core region of the disc as $r \to 0$. In this limit axisymmetry requires that $\varepsilon_{rr} = \varepsilon_{\theta\theta}$ and $\sigma_{rr} = \sigma_{\theta\theta}$ as the r and $\theta-$directions are indistinguishable. Then from (4.4) and (4.5) it follows that $\varepsilon_{rr}^{s} = \varepsilon_{\theta\theta}^{s}$ and thus in the limit $r \to 0$ the only admissible solution is $\ell = 0$ with $\varepsilon_{rr}^{s} = \varepsilon_{\theta\theta}^{s} = e^{[1]} = e^{[2]}$. Given this constraint we shall subsequently show that for all combinations of $\varepsilon_{zz}(r) = \varepsilon_0$ and $\langle\xi\rangle$, there exist only 3 types of solutions as sketched in Fig. 5a:

Regime I: A single phase with $\ell = 0$ over $0 \leq r \leq R$ with the $e^{[3]}$ direction aligned with the $z-$direction.

Regime II: A heterogeneous 2 domain solution with $\ell = 0$ over $0 \leq r \leq b$ and $\ell = 1$ in the outer shell $b < r \leq R$ such that the $e^{[3]}$ direction is now aligned with the $\theta-$direction so that $\varepsilon_{rr}^{s} = \varepsilon_{zz}^{s}$.

Regime III: A heterogeneous 2 domain solution with $\ell = 0$ over $0 \leq r \leq b$ and $\ell = 2$ in the outer shell $b < r \leq R$ such that the $e^{[3]}$ direction is now aligned with the $r-$direction so that $\varepsilon_{\theta\theta}^{s} = \varepsilon_{zz}^{s}$.

In regimes II and III, the transition radius b depends on $(\varepsilon_0, \langle\xi\rangle)$ and the stresses and mobile phase concentrations vary over $b < r \leq R$. On the other hand, in the core region over $0 \leq r \leq b$ the fields are spatially uniform. We proceed to demonstrate the spatial uniformity of the fields in the core region with $\ell = 0$. For $\ell = 0$, the equation for the chemical potential (4.7) reduces to

$$\mu = \frac{k}{c_R}(\sigma_{rr} + \sigma_{\theta\theta} - \sigma_{zz}) + \mathcal{R}\mathcal{T} \ln\left(\frac{\xi}{1-\xi}\right). \tag{4.8}$$

Chemical equilibrium implies $\partial\mu/\partial r = 0$ and thus we need to calculate the gradients of stresses $\partial\sigma_{rr}/\partial r$, $\partial\sigma_{\theta\theta}/\partial r$ and $\partial\sigma_{zz}/\partial r$. Substituting the constitutive relations (4.4)-(4.6) into the equilibrium equation (4.3) and using the compatibility relation

$$r\frac{\partial\varepsilon_{\theta\theta}}{\partial r} = \varepsilon_{rr} - \varepsilon_{\theta\theta}, \tag{4.9}$$

we obtain

$$r\frac{\partial^2\sigma_{rr}}{\partial r^2} + 3\frac{\partial\sigma_{rr}}{\partial r} = -\frac{E}{1-\nu^2}\left(\frac{\partial\varepsilon_{\theta\theta}^{s}}{\partial r} + \nu\frac{\partial\varepsilon_{zz}^{s}}{\partial r}\right), \tag{4.10}$$

where we have used the fact that $\partial\varepsilon_{zz}/\partial r = 0$. Integrating (4.10) we obtain

$$\frac{\partial\sigma_{rr}}{\partial r} = \frac{B}{r^3} - \frac{E}{1-\nu^2}\frac{1}{r^3}\int\frac{\partial\varepsilon_{\theta\theta}^{s}}{\partial r}r^2\mathrm{d}r - \frac{E\nu}{1-\nu^2}\frac{1}{r^3}\int\frac{\partial\varepsilon_{zz}^{s}}{\partial r}r^2\mathrm{d}r, \tag{4.11}$$

with B an integration constant. The requirement that σ_{rr} is finite at $r = 0$ implies $B = 0$ and thus

$$\frac{\partial \sigma_{rr}}{\partial r} = -\frac{E}{1-\nu^2}\frac{1}{r^3}\int \frac{\partial \varepsilon_{\theta\theta}^{s}}{\partial r} r^2 \mathrm{d}r - \frac{E\nu}{1-\nu^2}\frac{1}{r^3}\int \frac{\partial \varepsilon_{zz}^{s}}{\partial r} r^2 \mathrm{d}r. \tag{4.12}$$

Then $\partial \sigma_{\theta\theta}/\partial r$ follows from the equilibrium equation (4.3) and (4.10) as

$$\begin{aligned}\frac{\partial \sigma_{\theta\theta}}{\partial r} = {} & \frac{E}{1-\nu^2}\frac{1}{r^3}\int \frac{\partial \varepsilon_{\theta\theta}^{s}}{\partial r} r^2 \mathrm{d}r + \frac{E\nu}{1-\nu^2}\frac{1}{r^3}\int \frac{\partial \varepsilon_{zz}^{s}}{\partial r} r^2 \mathrm{d}r \\ & -\frac{E}{1-\nu^2}\frac{\partial \varepsilon_{\theta\theta}^{s}}{\partial r} - \frac{E\nu}{1-\nu^2}\frac{\partial \varepsilon_{zz}^{s}}{\partial r}.\end{aligned} \tag{4.13}$$

Substituting (4.12) and (4.13) in the constitutive relation (4.6) and recalling that $\partial \varepsilon_{zz}/\partial r = 0$ it follows that

$$\frac{\partial \sigma_{zz}}{\partial r} = -\frac{E\nu}{1-\nu^2}\frac{\partial \varepsilon_{\theta\theta}^{s}}{\partial r} - \frac{E}{1-\nu^2}\frac{\partial \varepsilon_{zz}^{s}}{\partial r}. \tag{4.14}$$

Then using (4.12)-(4.14) along with (4.8), it follows that a constant chemical potential implies

$$\left(\frac{2k^2 E}{c_R(1+\nu)} + \mathcal{R}\mathcal{T}\frac{1}{\xi(1-\xi)}\right)\frac{\partial \xi}{\partial r} = 0. \tag{4.15}$$

This holds for all ξ and hence chemical equilibrium implies $\partial \xi/\partial r = 0$, i.e. ξ is independent of r in the core region with $\ell = 0$. Therefore, the swelling strains are spatially uniform and from (4.12)-(4.14) it follows that $\partial \sigma_{rr}/\partial r = \partial \sigma_{\theta\theta}/\partial r = \partial \sigma_{zz}/\partial r = 0$ such that the stresses are also spatially uniform. This argument also implies that the solution in regime I is also spatially uniform with $\sigma_{rr} = 0$ from the boundary condition $\sigma_{rr} = 0$ at $r = R$. It then follows from (4.3) that $\sigma_{\theta\theta} = 0$.

4.4 Overview of solution method

The solution of the governing equations outlined above was obtained in a two-step process for a given loading specified by $\varepsilon_{zz}(r) = \varepsilon_0$ and $\langle \xi \rangle$. For a given assumed distribution $\ell(r)$ we solved the mechanical and chemical equilibrium conditions detailed in Sections 4.1 and 4.2 to obtain the associated equilibrium displacement field $u(r)$ and occupancy field $\xi(r)$. As a second step, the minimisation (3.8) was conducted to determine the distribution $\ell(r)$ that gives the lowest potential energy. We now discuss this two-step process in more detail.

First consider the mechanical and chemical equilibrium of the disc for a given $\ell(r)$. Inverting (4.4)-(4.6), the stresses σ_{rr}, $\sigma_{\theta\theta}$ and, σ_{zz} are written in terms of the swelling strains and the imposed $\varepsilon_{zz} = \varepsilon_0$ as

$$\sigma_{rr} = \lambda[(1-\nu)\varepsilon_{rr} + \nu\varepsilon_{\theta\theta}] + \lambda[\nu\varepsilon_0 - (1-\nu)\varepsilon_{rr}^{s} - \nu(\varepsilon_{\theta\theta}^{s} + \varepsilon_{zz}^{s})], \tag{4.16}$$

$$\sigma_{\theta\theta} = \lambda[(1-\nu)\varepsilon_{\theta\theta} + \nu\varepsilon_{rr}] + \lambda[\nu\varepsilon_0 - (1-\nu)\varepsilon_{\theta\theta}^{s} - \nu(\varepsilon_{rr}^{s} + \varepsilon_{zz}^{s})], \tag{4.17}$$

and

$$\sigma_{zz} = \lambda[(1-\nu)(\varepsilon_0 - \varepsilon_{zz}^{s}) + \nu(\varepsilon_{rr} + \varepsilon_{\theta\theta} - \varepsilon_{rr}^{s} - \varepsilon_{\theta\theta}^{s})]. \tag{4.18}$$

We discretised the 1D axisymmetric domain into $n-1$, 2-node elements with linear interpolation fields, i.e. constant strain elements. The displacement u_i^* $(i = 1, \cdots, n)$ are the unknowns at the nodes and given that $u_1^* = 0$ at $r = 0$, this implies $n-1$ unknowns. The weak form of the equilibrium equation (4.3) along with the definitions $\varepsilon_{rr} = du/dr$ and $\varepsilon_{\theta\theta} = u/r$ were used to setup $(n-1)$ equations for the displacement unknowns. These equations can be written in the form

$$K_{ij}u_j^* = g_i, \tag{4.19}$$

where K_{ij} is a stiffness matrix and g_i a vector of body forces that arise from the second bracket in (4.16) and (4.17), i.e. are functions of the occupancy ξ, orientation ℓ and the imposed strain ε_0.

The strains $(\varepsilon_{rr}, \varepsilon_{\theta\theta})$ are constant in the $n-1$ elements. Thus, to keep the swelling strains consistent with the total strains we set the occupancy ξ and orientation ℓ to be elemental variables and thus constant within the elements. Given ℓ^* in the $n-1$ elements, to solve (4.19) the occupancies ξ^* in the $n-1$ elements are also required. Additional equations are obtained by recalling that chemical equilibrium dictates that the chemical potential (4.7) is spatially uniform. Substituting (4.16)-(4.18) into (4.7) we setup an additional $n-2$ equations by equating the chemical potentials of adjacent elements, i.e. $\mu_{i+1}^* - \mu_i^* = 0$, where μ_i^* is the chemical potential of the i^{th} element. The constraint on the overall amount of the mobile phase as expressed by (4.1) provides the final equation and thus we have a total of $2n-2$ non-linear equations for the $n-1$ unknown nodal displacements u_i^* and the $n-1$ elemental occupancies ξ^*. We solve these equations simultaneously using the non-linear equation solver `fsolve` in MATLAB.

We next need to determine the distribution ℓ^* at equilibrium. In the context of uniaxial compression considered here, $T_i^0 = 0$ at $r = R$ and thus (3.7) reduces to

$$F(u_i, c, \ell) = \int_\Omega f d\Omega. \tag{4.20}$$

Denote F_ℓ as the value F for distributions $u(r)$ and $c(r)$ that satisfy mechanical and chemical equilibrium for a given distribution $\ell(r)$ and the imposed $(\varepsilon_0, \langle\xi\rangle)$. This is obtained using the non-linear solution procedure described above. The optimal or overall equilibrium solution corresponds to the minimisation over all possible distributions $\ell(r)$ as expressed by (3.8). In uniaxial context analysed here this reduces to

$$F_{\min} = \min_\ell F_\ell. \tag{4.21}$$

We performed extensive numerical experimentation to investigate possible distributions ℓ^* for a range of choices $(\varepsilon_0,\langle\xi\rangle)$ of the imposed loading. These investigations revealed that only the 3 regimes outlined in Section 4.3 minimise F_ℓ. The minimisation problem (4.21) therefore simplifies considerably and reduces to calculating solutions for 3 regimes for a given $(\varepsilon_0, \langle\xi\rangle)$. The solution for regime I is trivial as it is spatially uniform. In regimes II and III, a range of spatially varying solutions exist for $0 < b \leq R$: $F_{\min}$ for the given $(\varepsilon_0, \langle\xi\rangle)$ then corresponds to the minimum value of F_ℓ over all these solutions in regimes II and III as well as the single solution of regime I. Of course, for solutions with $F_{\min}$ in either regime II and III, the value of b at which the orientation switches from $\ell = 0$ to either $\ell = 1$ or $\ell = 2$ is also a direct outcome of the minimisation.

5. Deformation-induced heterogeneity under uniaxial loading

Recall our original aim of attempting to understand the deformation-induced heterogeneity seen on the central symmetric horizontal plane in Fig. 2b. On this plane, the imposed strain $\varepsilon_{zz} = \varepsilon_0$ is known and spatially uniform. However, the plane interacts with the rest of the cylindrical specimen and thus the average occupancy of the mobile phase $\langle\xi\rangle$ on that central plane depends on the imposed global loading and geometry of the specimen. We now proceed to investigate the development of heterogenous deformation as a function of $(\varepsilon_0, \langle\xi\rangle)$.

There are five key material parameters in the model. Two parameters are related to the elasticity of the crosslinked polymer network viz. the Young's modulus E and Poisson's ratio ν and three parameters are associated with the mobile phase which are the occupancy ξ_0 in the undeformed state, the concentration c_R of the sites of the mobile molecules and the non-dimensional parameter k that relates the swelling strains to the occupancy. The parameter c_R always appears with $\mathcal{RT}$ and thus we only specify the $\mathcal{RT}c_R$ which has units of stress. Unless otherwise specified we use the parameters listed in Table 1 which, except for ν, follow closely those of Wang et al. (2024). We set $\nu = 0.499$ so that the rubber is elastically nearly incompressible such that all volume changes are associated with the swelling strains due to the mobile phase.

Table 1: The reference material properties used in the calculations.

E	ν	k	$\mathcal{RT}c_R$	ξ_0
1.26 MPa	0.499	2	0.2 MPa	0.05

5.1 Overview of the solutions of the 3 regimes

The nature of solutions over the full space of $(\varepsilon_0, \langle\xi\rangle)$ is rich and complex and we first provide some illustrative examples of solutions in the three regimes described in Section 4.3. Restricting ourselves to $\langle\xi\rangle - \xi_0 = 0.025$ we select three values of $\varepsilon_0 = 0.03$, -0.02, and -0.1 which correspond to equilibrium solutions in regimes I, III and II, respectively.

First consider the case of $\varepsilon_0 = 0.03$ where the system attains equilibrium with a regime I solution. As demonstrated in Section 4.3, the solution in regime I is spatially uniform. The predicted variations of ξ, the three normalised stresses $(\sigma_{rr}/E, \sigma_{\theta\theta}/E, \sigma_{zz}/E)$, and the total strains $(\varepsilon_{rr}, \varepsilon_{\theta\theta})$ are included in Fig. 5b. The spatial uniformity of ξ implies that the swelling strains $(\varepsilon_{rr}^s, \varepsilon_{\theta\theta}^s, \varepsilon_{zz}^s)$ are spatially uniform and we get spatially uniform uniaxial solution with $\sigma_{rr} = \sigma_{\theta\theta} = 0$. Next consider the regime III solution with a compressive strain $\varepsilon_0 = -0.02$ (Fig. 5c). Here we have a spatially heterogeneous solution with $\varepsilon_{\theta\theta}^s = \varepsilon_{zz}^s$ in an outer shell $b < r < R$. For the choice $\varepsilon_0 = -0.02$, $b = 0.25R$ and ξ is discontinuous at $r = b$ with a sudden decrease in concentration ξ. Equilibrium and compatibility respectively demand that σ_{rr} and $\varepsilon_{\theta\theta}$ are continuous at the interface $r = b$ but the other components of stress and strain jump at the interface (since there is a jump in ξ at $r = b$ all components of the swelling strains are discontinuous at that interface). The solution switches to regime II for the larger imposed compressive strain $\varepsilon_0 = -0.1$ (Fig. 5d) where now we get a spatially heterogeneous solution with $\varepsilon_{rr}^s = \varepsilon_{zz}^s$ in an outer shell $b = 0.3R < r < R$. While again ξ is discontinuous at $r = b$ and σ_{rr} and $\varepsilon_{\theta\theta}$ are continuous, the main difference with the regime III solution is that the jump in ξ is positive with ξ increasing from $r = b^-$ to $r = b^+$ and the stresses decreasing in the outer shell $b < r < R$ with increasing r. While these three solutions give a flavour of the solutions in the 3 regimes, a richer set of responses are predicted over all combinations of $(\varepsilon_0, \langle\xi\rangle)$ as we now proceed to illustrate.

5.2 Phase diagram for deformation-induced heterogeneity

Clearly, the combination of loading $(\varepsilon_0, \langle\xi\rangle)$ strongly affects whether deformation induces heterogeneity and the type of heterogeneity that develops. To fully investigate this we map out the regimes of behaviour over a practical range of loading parameters, viz. $-0.3 \le \varepsilon_0 \le 0.3$

and $-0.05 \leq \langle\xi\rangle - \xi_0 \leq 0.05$ (recall $\xi_0 = 0.05$ and thus $\langle\xi\rangle - \xi_0 = -0.05$ is the lowest admissible value). Calculations were performed for approximately 3000 combinations of $(\varepsilon_0, \langle\xi\rangle)$ to calculate equilibrium solutions and thereby also determine the regimes of behaviour at each combination of $(\varepsilon_0, \langle\xi\rangle)$. A phase map with axes of $\langle\xi\rangle - \xi_0$ and ε_0 that indicates the regimes of behaviour is the outcome of these calculations and is included in Fig. 6. The map is dominated by regime II and to a lesser extend regime I with heterogeneity corresponding to regime III occurring over a narrow regime around $\varepsilon_0 \approx 0$. Most intriguingly, we observe that for $\langle\xi\rangle - \xi_0 = 0$, any imposed deformation results in nematic domain formation with the behaviour in regime II, i.e. nematic domain formation can occur even if the overall concentration remains at the reference value and occurs purely due to the imposition of mechanical loading. By contrast, for all values of $\langle\xi\rangle$, the equilibrium solutions are in regime I for $\varepsilon_0 = 0$. This is not a trivial result as the stress σ_{zz} is not zero for $\langle\xi\rangle - \xi_0 \neq 0$. This clearly demonstrates that mechanical loading or rather straining is required to induce heterogeneity.

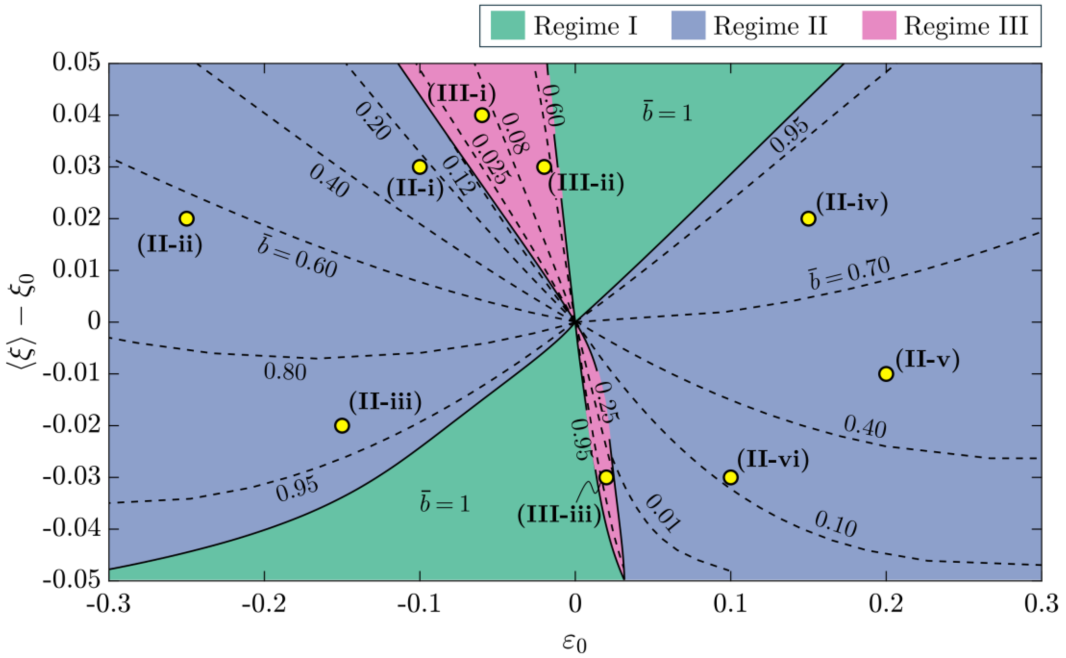

Figure 6: A phase map with axes of average occupancy parameterised by $\langle\xi\rangle - \xi_0$ and imposed axial strain ε_0. The map shows the regions over which the 3 regimes of deformation exist along with contours of the normalised transition radius $\bar{b}$ at which the orientation of the mobile phase molecules switches to result in a spatially heterogeneous solution. Locations at which detailed distributions of the fields are shown in Fig. 7 are also indicated.

Contours of the value of the non-dimensional radius $\bar{b} \equiv b/R$ are also included in Fig. 6. Of course, $\bar{b} = 1$ in regime I, as the solution in this regime is homogeneous with the mobile phase molecules in the $\ell = 0$ orientation over the entire domain. While this map shows the regimes of behaviour together with the associated transition radii, it does not directly provide information on the nature of the heterogeneity in the various regimes. We now proceed to discuss these heterogeneities. For the sake of brevity, we restrict the discussion to the spatial distribution of ξ, as the stresses and strains follow directly from ξ.

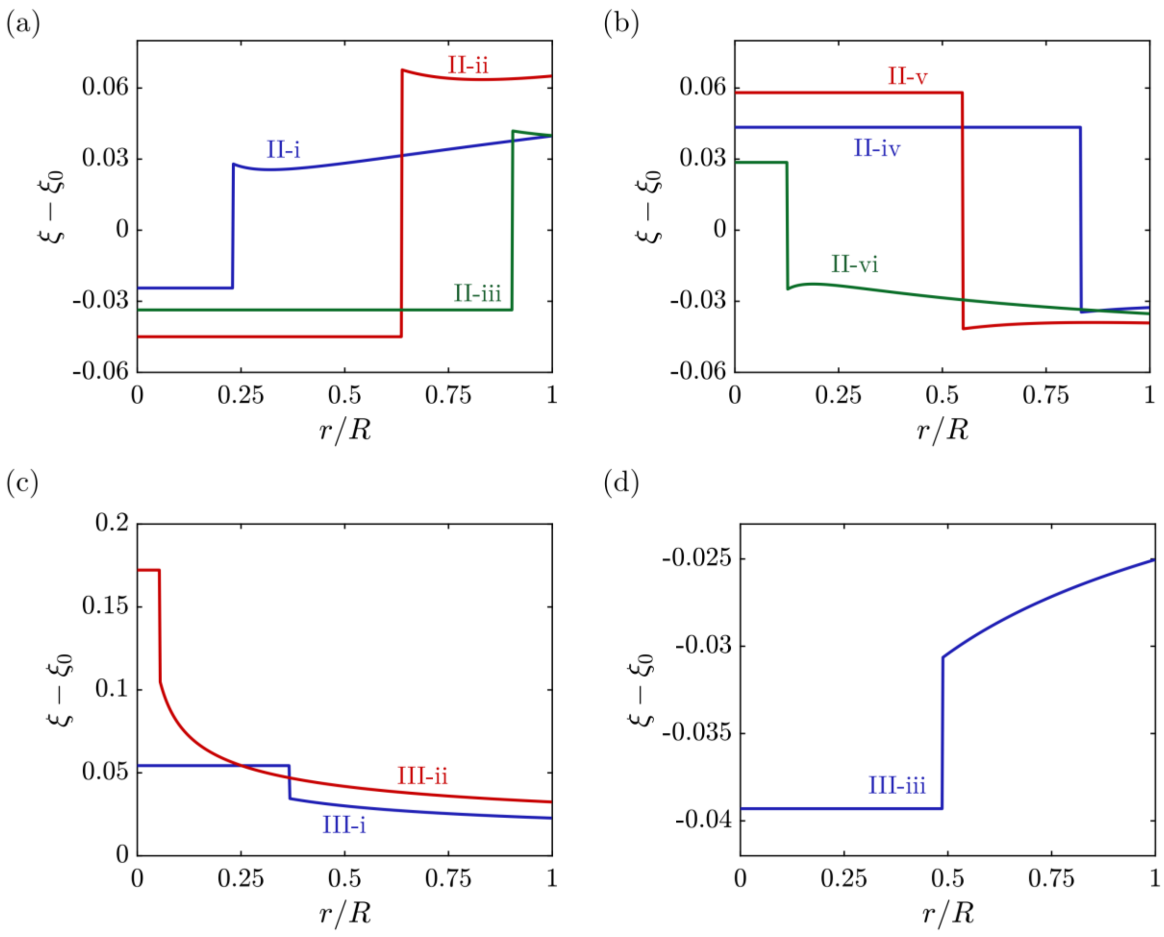

Figure 7: Distributions of the mobile phase concentration parameterised by $\xi - \xi_0$ as a function of the normalised radial position r/R at selected marked locations in the phase map in Fig. 6. Distributions in regime II for (a) compressive loading with $\varepsilon_0 < 0$ and (b) tensile loading with $\varepsilon_0 > 0$. Corresponding distributions in regime III for (c) compressive loading with $\varepsilon_0 < 0$ and (d) tensile loading with $\varepsilon_0 > 0$.

First consider regime II for $\varepsilon_0 < 0$. The distributions of ξ at three locations marked II-i to II-iii in Fig. 6 are included in Fig. 7a. In all cases the concentration in the core $0 \leq r \leq b$ is lower than the outer shell with $\xi - \xi_0$ switching sign from the core to the outer shell. Recalling that the volumetric strain is given by (3.1), the results in Fig. 7a indicate that the swelling strains induce dilation in the core and volumetric loss in the outer shell. Moreover, since the elastic volumetric strains are negligible, the total volumetric strains will display similar behaviour. These results suggest that our measurements (Fig. 2b) lie in the compressive regime II. Now consider tensile loading ($\varepsilon_0 > 0$) in regime II. Distributions of ξ are shown in Fig. 7b for the three locations marked II-iv to II-vi in Fig. 6. Under tensile loading the behaviour is switched with the concentration in the core $0 \leq r \leq b$ higher than the outer shell and again $\xi - \xi_0$ switching sign from the core to the outer shell. Thus, under tensile loading the core undergoes a volumetric loss while the outer shell dilates.

The prediction that an imposed compressive loading results in dilation in the core and vice-versa under tensile loading is however not a universal result. Now consider regime III for $\varepsilon_0 < 0$ with the distributions of ξ shown in Fig. 7c for the two locations marked III-i and III-ii in Fig. 6. Two key differences are observed compared to the compressive loading results shown in Fig. 7a. First, $\xi - \xi_0$ is higher in the core region $0 \leq r \leq b$ and throughout the domain $\xi - \xi_0 > 0$ such that there is volumetric loss for all r. Regime III for $\varepsilon_0 > 0$ is a narrow regime and we consider only the point labelled III-iii in Fig. 6. The distribution included in Fig. 7d shows that in this case $\xi - \xi_0$ is lower in the core region $0 \leq r \leq b$ and that throughout the domain $\xi - \xi_0 < 0$, i.e. the entire disc undergoes dilation. In summary, the regime and the sign of the imposed ε_0 together govern the nature of the heterogeneity. We note in passing that while both regimes II and III correspond to spatially heterogeneous distributions, the mixture of dilation and volumetric loss as observed in the measurements (Fig. 2b) only occurs in regime II. Our observations and the measurements of Wang et al. (2024) will be discussed in more details in Section 5.4 in the context of the phase map of Fig. 6.

5.3 Types of phase transitions

Contours of the normalised transition radius $\bar{b}$ included in Fig. 6 show that $\bar{b}$ is continuous across the boundaries of regimes I and II as well as regimes I and III. However, $\bar{b}$ is discontinuous across the boundaries of regimes II and III. To understand this discontinuity, consider the case with $\langle \xi \rangle - \xi_0 = -0.04$ over the range of imposed strains $-0.3 \leq \varepsilon_0 \leq 0.3$. The variation of $\bar{b}$ with ε_0 is included in Fig. 8a (the different regimes are indicated). The discontinuity in $\bar{b}$ across the regime II and III boundary is clear and shown by the straight black line. To understand the nature of this discontinuity, we consider in Fig. 8b the corresponding variation of the normalised equilibrium free energy $\bar{F}_{\min} \equiv F_{\min}/(ER^2)$. While $\bar{F}_{\min}$ is of course continuous, its gradient with respect to ε_0 is discontinuous across the regime II and III boundary (this is further clarified in the zoom-in in Fig. 8b). The discontinuity of this gradient is not only directly associated with the discontinuity in $\bar{b}$ but is also reflected in more directly measurable quantities such as the work-conjugate to the applied ε_0, viz. the average applied force given by

$$\langle \sigma_{zz} \rangle \equiv \frac{2}{R^2} \int_0^R \sigma_{zz} \, r dr. \tag{5.1}$$

The corresponding variation in the normalised stress $\langle \sigma_{zz} \rangle / E$ with ε_0 is included in Fig. 8c with the zoom-in clearly showing that the average force is discontinuous across the regime II-III boundary. The abrupt change in a thermodynamic property such as the average force follows from the discontinuity in the first derivative of free energy and shows that a first-order phase transition is occurring across the regime II-III boundary. No first-order phase transitions are evident across the other boundaries with all thermodynamic properties varying continuously across those boundaries.

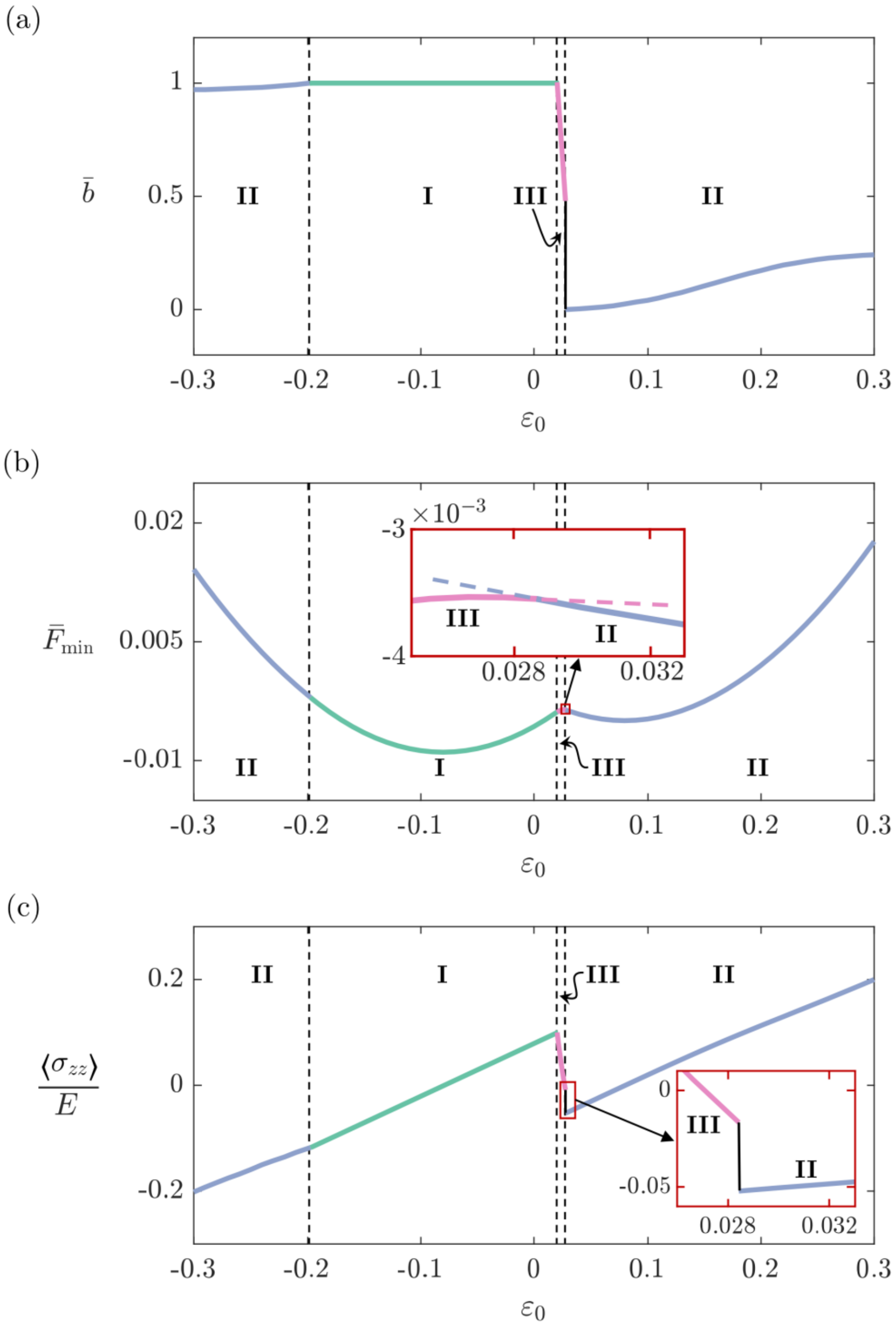

Figure 8: Variation of key macroscopic quantities with ε_0 to understand the types of transitions across the regime boundaries. The variation of (a) normalised transition radius $\bar{b}$, (b) normalised free energy $\bar{F}_{\min}$ and (c) average force $\langle \sigma_{zz} \rangle / E$ with ε_0 for $\langle \xi \rangle - \xi_0 = -0.04$. The regimes of behaviour are indicated in each case. In (a) and (c) the discontinuity of $\bar{b}$ and $\langle \sigma_{zz} \rangle / E$ across the regime II-III boundary is indicated by a straight black line with zoom-ins also included in (b) and (c) to illustrate the discontinuity in the gradient of $\bar{F}_{\min}$ with ε_0 and the discontinuity in $\langle \sigma_{zz} \rangle$ across the regime II and III boundary.

5.4 Experimental measurements & observed regimes of behaviour

The phase map (Fig. 6) illustrates a rich diversity of responses. Do measurements support such predictions? Our measurements (Fig. 2b) and the measurements of Wang et al. (2024) are now employed to judge the fidelity of the predictions.

Wang et al. (2024) conducted tensile tests on cylindrical specimens of varying aspect ratio H/D that were glued to platens. The spatial distributions of the volumetric strain $\left[\det(F_{ij}) - 1\right]$ from these measurements at three values of the applied nominal strains U/H are included in Fig. 9 for specimens with aspect ratio $H/D = 1$ (Fig. 9a) and 2 (Fig. 9b). The corresponding spatial variations of the axial component of the deformation gradient F_{33} are also included in Figs. 9a and 9b. The associated variations on the central plane (marked as sections AA and BB in Figs. 9a and 9b, respectively) indicate that the volumetric strains vary with r but the axial deformation parameterised by F_{33} is spatially uniform. We can use these measurements to gauge the regime of behaviour on the central plane of the specimens. The phase map in Fig. 6 has axes of $\langle\xi\rangle - \xi_0$ and ε_0. We can approximate ε_0 as $\varepsilon_0 \approx F_{33} - 1$. Similarly, recall that $\varepsilon_{ii}^{s} = -k(\xi - \xi_0)$. Then assuming that all the measured volumetric strain is solely due to the swelling strains (i.e. elastic volumetric strains are negligible consistent with our choice of $\nu = 0.499$), we can estimate $\langle\xi\rangle - \xi_0$ as

$$\langle\xi\rangle - \xi_0 = \frac{2}{kR^2}\int_0^R \left[1 - \det(F_{ij})\right] r dr, \tag{5.2}$$

where $\det(F_{ij})$ is obtained from measurements. We can now use the data from Fig. 9 to plot trajectories of the measurements of Wang et al. (2024) on the phase map and these are included in Fig. 10a. The trajectory of the $H/D = 1$ specimen shows an increase in $\langle\xi\rangle - \xi_0$ with increasing deformation as the volume of the central plane reduces under imposed tensile loading. On the other hand, $\langle\xi\rangle - \xi_0$ is closer to zero for the $H/D = 2$ case indicating a smaller change in volume of the central plane in this higher aspect ratio specimen. These observations can be understood as follows. For a long specimen, the effect of the glued platens is not felt towards the central plane with all circular section planes near the centre will behave almost identically. This constrains long specimens to obey $\langle\xi\rangle - \xi_0 = 0$ around the central plane. The measurements suggest that the $H/D = 2$ approaches this long specimen limit. On the other hand, the effect of the glued platens pervades throughout the $H/D = 1$ specimen and $\langle\xi\rangle - \xi_0 \neq 0$ on the central plane. We can now test the key prediction of regime II that under tensile loading the specimen loses volume in the central core and dilates in an outer shell.

Consider the final deformed states of the $H/D = 1$ and 2 specimens under tension. Both states correspond to approximately the same value of ε_0 but $\langle\xi\rangle - \xi_0$ is much lower for the $H/D = 2$. The predictions of the spatial variations of the volumetric strains ε_{ii} as a function of the normalised radial position r/R are included in Fig. 10b and are in qualitative agreement with the measurements; viz. the inner core of the disc $0 \leq r < b$ loses volume while the outer shell gains volume. Most intriguingly, in line with the observations in Fig. 9, spatial inhomogeneity develops in the $H/D = 2$ case even though $\langle\xi\rangle - \xi_0$ is only about 0.2%. This bears out the intriguing prediction in Fig. 6 that straining results in spatially non-uniform deformation even with $\langle\xi\rangle - \xi_0 = 0$.

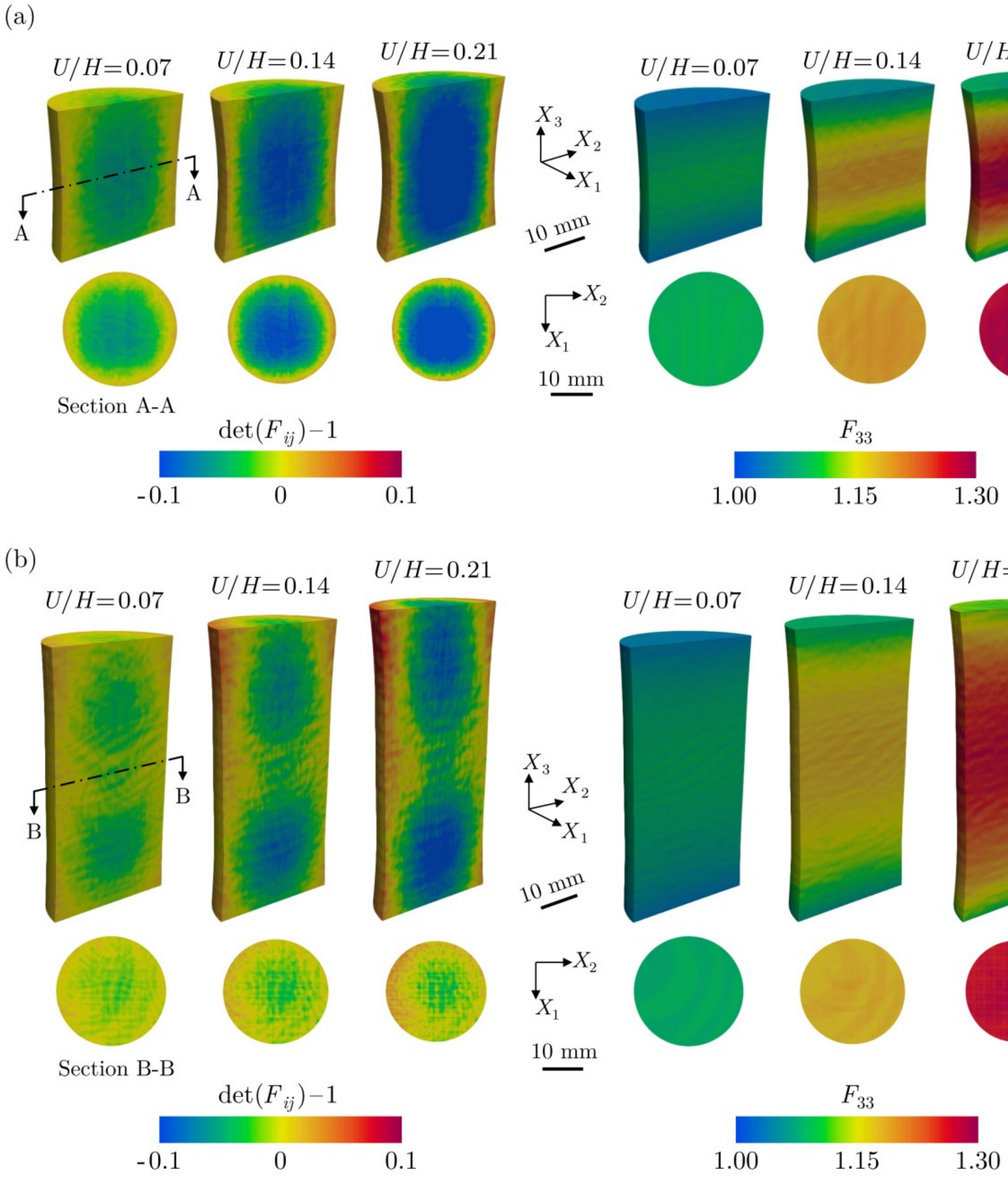

Figure 9: Measurements of the spatial distributions of volumetric strain $\det(F_{ij})-1$ and axial deformation gradient F_{33} at three levels of applied tensile nominal strain U/H for the (a) $H/D=1$ and (b) $H/D=2$ cylindrical specimens. Results are reproduced from Wang et al. (2024). The distributions are shown on the diametrical and the central planes of the specimens.

Next consider compressive loading of the $H/D=1$ and 2 specimens. The spatial distributions of $\left[\det(F_{ij})-1\right]$ and F_{33} over these specimens at three values of the applied nominal strains U/H are shown in Figs. 2b and 2c and in Wang et al. (2024), respectively. The corresponding deformation trajectories of the central plane are included in Fig. 10a and the corresponding predictions of the spatial variations of ε_{ii} are included in Fig. 10c for the final deformed states. The situation is swapped with the central core undergoing dilation and the outer shell losing volume. This is in line with the observations in Figs. 2b and 2c and in Wang et al. (2024). The corresponding predictions of the change in the mobile phase concentrations $\xi-\xi_0$ are also included in Fig. 10c: consistent with the observations in Figs. 3b and 3c, the predictions suggest that under compressive loading the mobile phase concentration reduces in the central core and increases in the outer shell.

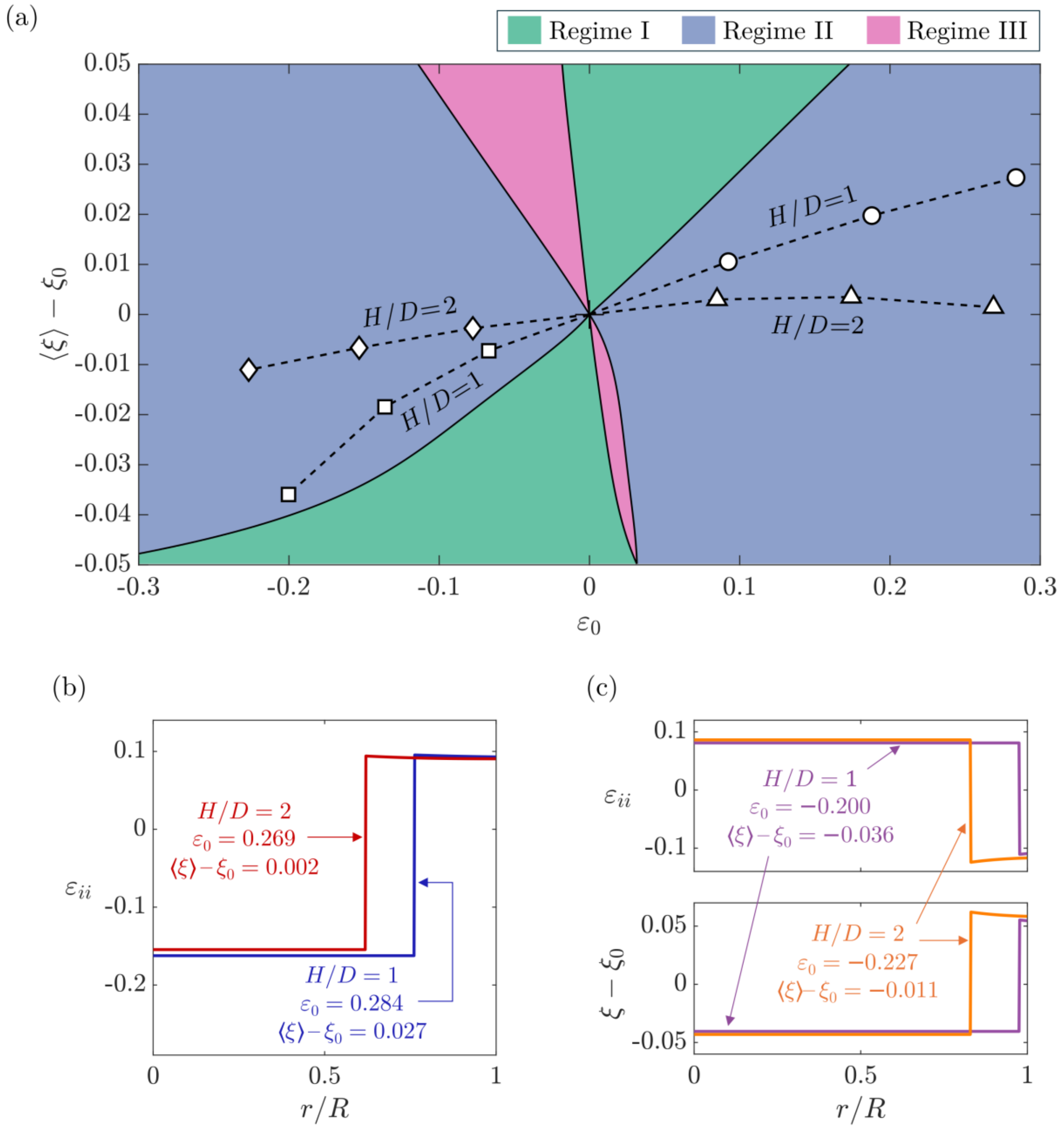

Figure 10: (a) Phase map of Fig. 6 with trajectories of four experiments: the tensile $H/D = 1$ and 2 tests from Fig. 9 and the compressive $H/D = 1$ and 2 tests from Figs. 2b and 2c and Wang et al. (2024), respectively. (b) Predictions of the variations of the volumetric strain ε_{ii} as a function of the normalised radial position r/R for the $H/D = 1$ and 2 specimens subjected to tensile loading. Results are shown for the final deformed states. (c) Predictions of the variations of ε_{ii} and the change in the mobile phase concentrations $\xi - \xi_0$ with r/R at the final deformed states of the compressively loaded $H/D = 1$ and 2 specimens.

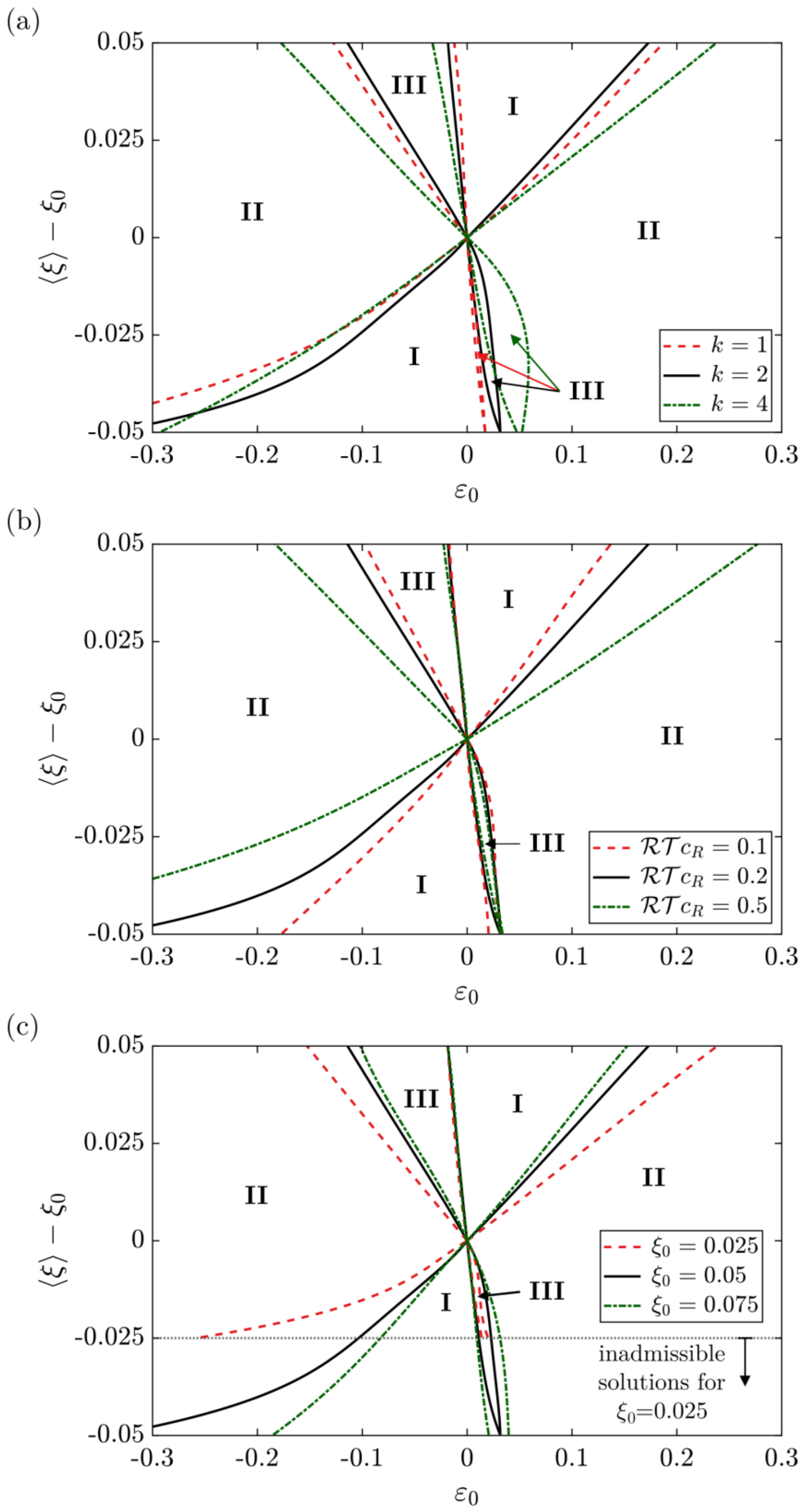

Figure 11: Phase maps to show the effect of mobile phase material properties on the regimes of response. In each case we show the boundaries between regimes for two values of material properties in addition to the reference values in Table 1. (a) Effect of varying k with $\mathcal{RT}c_R$ and ξ_0 held fixed at reference values. (b) Effect of varying $\mathcal{RT}c_R$ with k and ξ_0 held fixed at reference values. (c) Effect of varying ξ_0 with k and $\mathcal{RT}c_R$ held fixed at reference values.

Overall, we have remarkable qualitative agreement between predictions and numerous counterintuitive observations. These include:

- (i) A mixture of dilation and volume loss under uniform imposed axial strain.
- (ii) A core region undergoing volume loss under tensile deformation and vice-versa under compressive loading
- (iii) The mobile phase concentration reduces in regimes undergoing dilation.

All these observations are predicted by the model which suggests that nematic domains of the mobile phase (corresponding to regime II in the map of Fig. 6) form in the central disc of the cylindrical specimens. However, while the predictions and observations are in good qualitative agreement, the model, unlike the measurements, predicts a sharp switch in the volumetric strain corresponding to nematic domain formation because of an abrupt change in the orientation of the mobile phase molecules. This discrepancy arises because the DVC were performed using 3D cubic splines to parameterise the displacement fields (D. Rueckert et al., 1999). This means that sharp gradients in the displacement fields are smeared out in the measurements. Nevertheless, the model correctly predicts deformation-induced heterogeneity, the signs of the volumetric strains, and the associated changes in the mobile phase concentrations.

5.5 Influence of material parameters

The predictions are in good qualitative agreement with observations which motivates us to understand the dependence of the predictions on material parameters. Three of the five parameters in Table 1 are related to the mobile phase and the uncertainty in the values of these parameters is the highest. We thus focus on understanding the effects of $k, \mathcal{R}\mathcal{T}c_R$ and ξ_0 on the phase map. We vary these parameters in turn keeping the others fixed at their reference values listed in Table 1.

The effect of k in the range $1 \le k \le 4$ is illustrated in Fig. 11a. Increasing k from 2 to 4 results in a slight expansion of the uniform (regime I) and regime III domains, with a corresponding contraction of regime II. However, decreasing k below 2 also results in an expansion of regimes I and III. This suggests that the domains of regimes I and III are of minimum size at $k \approx 2$. The effect of $\mathcal{R}\mathcal{T}c_R$ is more monotonic as seen in Fig. 11b, viz. the domains of regimes I and III increase with increasing $\mathcal{R}\mathcal{T}c_R$. Fig. 11c shows the effect of varying ξ_0: with increasing ξ_0, the domains of regimes I and III shrink (note that for $\xi_0 = 0.025$, the map is constrained to values of $\langle\xi\rangle - \xi_0 \ge -0.025$). There are three key messages from this material parametric study:

- (i) No new regimes of behaviour are introduced over the realistic range of parameters explored here.
- (ii) In all cases, the solution remains in regime I for $\varepsilon_0 = 0$. This reinforces the statement that the development of heterogeneity requires imposed straining.
- (iii) In all cases, deformation induces heterogeneity corresponding to regime II for $\langle\xi\rangle - \xi_0 = 0$.

6. Concluding discussion

X-ray measurements of the three-dimensional spatial volumetric strain fields demonstrate that silicone rubber specimens undergo heterogeneous deformation even if they are subjected to spatially uniform tensile/compressive straining. Our observations show that under uniform imposed axial compressive strains, the rubber gains volume in a central core region and loses volume in an outer shell. Using a ZnI_2 dopant, we demonstrated that this heterogeneity is associated with the motion of a mobile phase within the rubber resulting in a reduction in the mobile phase concentration in the core region where we observe a volume gain. These counterintuitive observations are rationalised by a model for the rubber that includes a mobile phase inducing anisotropic swelling strains. A direct outcome of the model is the prediction of the formation of nematic domains of the mobile phase within the rubber (akin to a liquid crystal). These domains induce heterogeneous deformation of the rubber even under uniform imposed axial deformation.

Phase maps with axes of mobile phase concentration and imposed axial strain are presented. These maps illustrate that under uniform imposed axial deformation there exist three regimes of behaviour including a regime where the rubber deforms in a spatially uniform manner. Consistent with observations the model predicts volume loss within the core of the cylindrical specimen and dilation in the outer shell under tensile loading (and vice versa under compressive loading). Moreover, the predictions are also in line with the observations of the motion of the mobile phase viewed using the $\mathrm{ZnI_2}$ dopant. Together our results strongly suggest that the observed heterogeneous deformation is a consequence of nematic domain formation within the silicone rubber.

Appendix A: Summary of the in situ X-ray measurements

The in-situ compression tests on the cylindrical specimens were conducted using the bespoke loading rig developed by Wang et al. (2024). X-ray tomographs were obtained using the Nikon XTH 225 ST system. X-rays were generated using a Tungsten source (target) operated at a tube voltage of 135 kVp and a tube current of 365 μA. The transmitted X-rays were captured on a 2000×2000 pixels CCD detector with a resolution of $150\,\mu\mathrm{m\,pixel}^{-1}$. Geometric magnification achieved via the location of the detector and sample stage relative to the X-ray source enhanced the resolution of the scans to 49 μm pixel^{-1}. A copper filter with a thickness of 0.5 mm was between the X-ray source and specimen to eliminate low-energy X-rays in the Bremsstrahlung spectrum and thereby reduce beam hardening effects at the specimen-air interface. We employed an exposure time of 2.83 s to strike a balance between a reasonable scan time (~90 minutes for 2053 projections) while also maintaining a high signal-to-noise ratio (the photon count through the specimen is at least 1.5 times the background noise of the detector). Tomographic reconstruction using scans of the 2053 projections was performed using a backpropagation algorithm and beam hardening corrections applied using polynomial curves to ensure that the mean deviation in grey values between the centre and the edge of the specimen was less than 10%. The resulting reconstructed volumes were exported as uncompressed .raw files and imported into VGStudioMax 2023.2.1 for post-processing analysis.

Appendix B: Regularisation of the free-energy for isotropic loading

The measurements of Wang et al. (2024) show that silicone rubber is initially isotropic. Thus, Wang et al. (2024) added a regularisation term to the free-energy to ensure a purely isotropic response in the absence of imposed deviatoric strains. However, this regularisation is insufficient given the assumed transversely isotropic swelling strains (3.2). Specifically, the principal swelling strains $\left(e^{[1]}, e^{[2]}, e^{[3]}\right)$ are such that $e^{[1]} = e^{[2]}$ and thus the response of the rubber should also be transversely isotropic for transversely isotropic loading.

To illustrate such transversely isotropic loading consider the pure bending of a bar under plane stress conditions as sketched in Fig. A1 with X_3 corresponding to the longitudinal direction. Pure bending implies that (X_1, X_2, X_3) are principal directions and plane stress implies that $\sigma_{22} = 0$. The boundary condition that the traction $T_1 = 0$ on the beam upper and lower surfaces

$X_1 = \pm h$ together with the stress equilibrium condition then dictates that $\sigma_{11} = 0$. Thus, the principal directions (X_1, X_2) are indifferentiable in terms of the imposed loading. Consequently, given the swelling strains (3.2), aligning $e^{[1]}$ and $e^{[2]}$ with X_1 and X_2 or vice-versa will imply that the response in the X_1 and X_2 directions are also identical. Any other choice of the orientations of the swelling strains will result in the response not only breaking the required symmetries but also resulting in a non-unique response as we now illustrate.

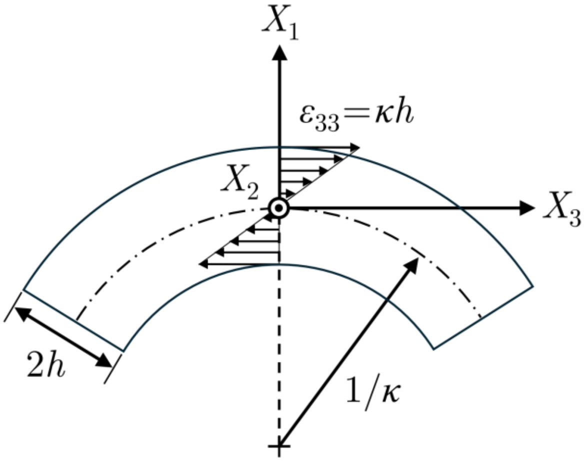

Figure A1: Sketch of pure bending with the global co-ordinate system indicated.

For example, consider the choice where $\left(e^{[1]}, e^{[2]}, e^{[3]}\right)$ are aligned with (X_3, X_1, X_2) such that the only unique swelling strain is now aligned with the X_2-direction. The strain ε_{11} will now not equal ε_{22} to ensure that $\sigma_{11} = \sigma_{22} = 0$. Another choice, where $\left(e^{[1]}, e^{[2]}, e^{[3]}\right)$ are aligned with (X_3, X_2, X_1) where the only unique swelling strain is now aligned with the X_1-direction will result in the same free-energy but with values of the strains ε_{11} and ε_{22} being swapped from the previous choice of the orientations of the swelling strains. In fact, our calculations showed that for this case of plane stress pure bending, all three orientations of the choices of the swelling strains result in the same free-energy but rather different deformation responses. A regularisation is needed to ensure uniqueness of the response and that required symmetries are obeyed. The regularisation needs to ensure that identical swelling strains are aligned with directions of identical loading.

To ensure that the identical swelling strains are aligned with directions of identical loading we specify the regularising term $f_{\text{reg}}(\varepsilon_{ij}, c, \ell)$ in (3.3) as follows. Let $\mathcal{E}^{[i]}$ denote principal total strains and $\Sigma^{[i]}$ the "anticipated" associated principal stresses. The elastic principal strains are $\mathcal{E}_e^{[i]} \equiv \mathcal{E}^{[i]} - e^{[i+\ell \,(\mathrm{mod}\, 3)]}$ and then $\Sigma^{[i]}$ are given by

$$\Sigma^{[1]} = \frac{E}{(1+\nu)(1-2\nu)}\left[(1-\nu)\mathcal{E}_e^{[1]} + \nu(\mathcal{E}_e^{[2]} + \mathcal{E}_e^{[3]})\right], \tag{A1}$$

$$\Sigma^{[2]} = \frac{E}{(1+\nu)(1-2\nu)}\left[(1-\nu)\mathcal{E}_e^{[2]} + \nu(\mathcal{E}_e^{[1]} + \mathcal{E}_e^{[3]})\right], \tag{A2}$$

and

$$\Sigma^{[3]} = \frac{E}{(1+\nu)(1-2\nu)}\left[(1-\nu)\mathcal{E}_e^{[3]} + \nu(\mathcal{E}_e^{[2]} + \mathcal{E}_e^{[1]})\right], \tag{A3}$$

i.e., $\Sigma^{[i]}$ are the stresses that follow from f with $f_{\text{reg}} = 0$. We then define f_{reg} as

$$f_{\text{reg}} = \sum_{\ell=0}^{2} \chi\lambda\left(e^{[\ell\ (\text{mod}\,3)]} - e^{[\ell+1\ (\text{mod}\,3)]}\right)^2$$

$$\left[\exp\left\{-\left(\frac{\Sigma^{[\ell\ (\text{mod}\,3)]} - \Sigma^{[\ell+1\ (\text{mod}\,3)]}}{\sigma_0}\right)^2\right\} + \exp\left\{-\left(\frac{\mathcal{E}^{[\ell\ (\text{mod}\,3)]} - \mathcal{E}^{[\ell+1\ (\text{mod}\,3)]}}{\varepsilon_0}\right)^2\right\}\right], \tag{A4}$$

where the parameters χ, σ_0, and ε_0 are positive regularisation constants. The constants σ_0 and ε_0 set the difference between the principal stresses and strains, respectively below which two principal directions are defined to have identical loading. In case the difference between either the anticipated stresses or total strains is below these critical values, the regularisation term is triggered with the magnitude of the regularisation energy set by the non-dimensional constant χ that scales the first Lamé constant λ. Choosing sufficiently small σ_0 and ε_0 as well as a large χ ensures that f_{reg} only serves as a regularisation term and is never triggered in all the results discussed in the main text.

Acknowledgements

The authors acknowledge funding from the UKRI Frontier Research grant “Graph-based Learning and Design of Advanced Mechanical Metamaterials” with award number EP/X02394X/1.

References

Arruda, E.M., Boyce, M.C., 1993. A three-dimensional constitutive model for the large stretch behavior of rubber elastic materials. Journal of the Mechanics and Physics of Solids 41, 389–412. https://doi.org/10.1016/0022-5096(93)90013-6

Bay, B.K., 2008. Methods and applications of digital volume correlation. The Journal of Strain Analysis for Engineering Design 43, 745–760. https://doi.org/10.1243/03093247JSA436

Bay, B.K., Smith, T.S., Fyhrie, D.P., Saad, M., 1999. Digital volume correlation: Three-dimensional strain mapping using X-ray tomography. Experimental Mechanics 39, 217–226. https://doi.org/10.1007/BF02323555

Bladon, P., Terentjev, E.M., Warner, M., 1994. Deformation–induced orientational transitions in liquid crystals elastomer. Journal de Physique II 4, 75–91.

Buljac, A., Jailin, C., Mendoza, A., Neggers, J., Taillandier-Thomas, T., Bouterf, A., Smaniotto, B., Hild, F., Roux, S., 2018. Digital Volume Correlation: Review of Progress and Challenges. Experimental Mechanics 58, 661–708. https://doi.org/10.1007/s11340-018-0390-7

D. Rueckert, L. I. Sonoda, C. Hayes, D. L. G. Hill, M. O. Leach, D. J. Hawkes, 1999. Nonrigid registration using free-form deformations: application to breast MR images. IEEE Transactions on Medical Imaging 18, 712–721. https://doi.org/10.1109/42.796284

Deuschle, J.K., Buerki, G., Deuschle, H.M., Enders, S., Michler, J., Arzt, E., 2008. In situ indentation testing of elastomers. Acta Materialia 56, 4390–4401. https://doi.org/10.1016/j.actamat.2008.05.003

Flory, P.J., 1944. Network Structure and the Elastic Properties of Vulcanized Rubber. Chem. Rev. 35, 51–75. https://doi.org/10.1021/cr60110a002

Flory, P.J., Rehner, J., Jr., 1943. Statistical Mechanics of Cross‐Linked Polymer Networks I. Rubberlike Elasticity. The Journal of Chemical Physics 11, 512‐520. https://doi.org/10.1063/1.1723791

Harkous, A., Colomines, G., Leroy, E., Mousseau, P., Deterre, R., 2016. The kinetic behavior of Liquid Silicone Rubber: A comparison between thermal and rheological approaches based on gel point determination. Reactive and Functional Polymers 101, 20–27. https://doi.org/10.1016/j.reactfunctpolym.2016.01.020

James, H.M., Guth, E., 1944. Theory of the Elasticity of Rubber. Journal of Applied Physics 15, 294–303. https://doi.org/10.1063/1.1707432

James, H.M., Guth, E., 1943. Theory of the Elastic Properties of Rubber. The Journal of Chemical Physics 11, 455–481. https://doi.org/10.1063/1.1723785

Jia, Y., Sun, S., Liu, L., Mu, Y., An, L., 2004. Design of silicone rubber according to requirements based on the multi-objective optimization of chemical reactions. Acta Materialia 52, 4153–4159. https://doi.org/10.1016/j.actamat.2004.05.029

Jose, K., Meng, Z., Dennis, A.R., Grega, I., Shaikeea, A.J.D., Deshpande, V.S., 2025. Exploration of digital volume correlation in nominally homogeneous metals. Mechanics of Materials 207, 105394. https://doi.org/10.1016/j.mechmat.2025.105394

Küpfer, J., Finkelmann, H., 1991. Nematic liquid single crystal elastomers. Die Makromolekulare Chemie, Rapid Communications 12, 717–726. https://doi.org/10.1002/marc.1991.030121211

Long, T.R., Elder, R.M., Bain, E.D., Masser, K.A., Sirk, T.W., Yu, J.H., Knorr, D.B., Lenhart, J.L., 2018. Influence of molecular weight between crosslinks on the mechanical properties of polymers formed via ring-opening metathesis. Soft Matter 14, 3344–3360. https://doi.org/10.1039/C7SM02407J

Mazurek, P., Vudayagiri, S., Skov, A.L., 2019. How to tailor flexible silicone elastomers with mechanical integrity: a tutorial review. Chem. Soc. Rev. 48, 1448–1464. https://doi.org/10.1039/C8CS00963E

Mooney, M., 1940. A Theory of Large Elastic Deformation. Journal of Applied Physics 11, 582–592. https://doi.org/10.1063/1.1712836

Rivlin, R.S., 1948. Large elastic deformations of isotropic materials. I. Fundamental concepts. Philosophical Transactions of the Royal Society of London, Series A: Mathematical and Physical Sciences 240, 459–490. https://doi.org/10.1098/rsta.1948.0002

Rivlin, R.S., Saunders, D.W., 1951. Large elastic deformations of isotropic materials VII. Experiments on the deformation of rubber. Philosophical Transactions of the Royal Society of London, Series A: Mathematical and Physical Sciences 243, 251–288. https://doi.org/10.1098/rsta.1951.0004

Scott, O.N., Begley, M.R., Komaragiri, U., Mackin, T.J., 2004. Indentation of freestanding circular elastomer films using spherical indenters. Acta Materialia 52, 4877–4885. https://doi.org/10.1016/j.actamat.2004.06.043

Stephen, M.J., Straley, J.P., 1974. Physics of liquid crystals. Rev. Mod. Phys. 46, 617–704. https://doi.org/10.1103/RevModPhys.46.617

Treloar, L.R.G., 1944. Stress-strain data for vulcanised rubber under various types of deformation. Trans. Faraday Soc. 40, 59–70. https://doi.org/10.1039/TF9444000059

Treloar, L.R.G., 1943a. The elasticity of a network of long-chain molecules. I. Trans. Faraday Soc. 39, 36–41. https://doi.org/10.1039/TF9433900036

Treloar, L.R.G., 1943b. The elasticity of a network of long-chain molecules—II. Trans. Faraday Soc. 39, 241–246. https://doi.org/10.1039/TF9433900241

Wang, Z., Das, S., Joshi, A., Shaikeea, A.J.D., Deshpande, V.S., 2024. 3D observations provide striking findings in rubber elasticity. Proceedings of the National Academy of Sciences 121, e2404205121. https://doi.org/10.1073/pnas.2404205121

Williams, R., 1963. Domains in Liquid Crystals. The Journal of Chemical Physics 39, 384–388. https://doi.org/10.1063/1.1734257

Zhang, Y., Zhang, Z., Huo, Y., 2020. Nucleation and critical conditions for stripe domains in monodomain nematic elastomer sheets under uniaxial loading. Journal of the Mechanics and Physics of Solids 144, 104110. https://doi.org/10.1016/j.jmps.2020.104110

Zhao, S., Chen, Y., Huo, Y., 2023. Formation of lamellar domains in liquid crystal elastomers under compression. International Journal of Mechanical Sciences 247, 108185. https://doi.org/10.1016/j.ijmecsci.2023.108185

Zubarev, E.R., Kuptsov, S.A., Yuranova, T.I., Talroze, R.V., Finkelmann, H., 1999. Monodomain liquid crystalline networks: reorientation mechanism from uniform to stripe domains. Liquid Crystals 26, 1531–1540. https://doi.org/10.1080/026782999203869